Surface Cyclogenesis from Convectively Driven Amplification of Midlevel Mesoscale Convective Vortices

ROBERT F. ROGERS

NOAA/AOML Hurricane Research Division, Miami, Florida

J. MICHAEL FRITSCH

Department of Meteorology, The Pennsylvania State University, University Park, Pennsylvania

(Manuscript received 8 December 1999, in final form 4 July 2000)

ABSTRACT

Mesoscale convective vortices (MCVs) are midtropospheric warm-core cyclonic circulations that often develop in the stratiform region of mesoscale convective systems. Typically, divergent, anticyclonically circulating, mesoscale cold anomalies appear both above and below the MCV. The upper-level cold anomaly is usually found near the tropopause while the low-level anomaly is surface based and exhibits locally higher pressure. One aspect of MCVs that has received much attention recently is the role that they may play in tropical cyclogenesis. Of special interest is how an MCV amplifies when deep convection redevelops within the borders of its midlevel cyclonic circulation and how the amplified MCV transforms the divergent surface-based cold pool with anomalously high surface pressure into a convergent cyclonic circulation with anomalously low pressure.

The Pennsylvania State University–National Center for Atmospheric Research fifth-generation Mesoscale Model is used to simulate an MCV that was instrumental in initiating, within the borders of the midlevel vortex's circulation, several successive cycles of convective development and decay over a 2-day period. After each cycle of convection, both the horizontal size of the cyclonic circulation and the magnitude of the potential vorticity associated with the vortex were observed to increase. The simulation reproduces the development and evolution of the MCV and associated convective cycles. Mesoscale features responsible for the initiation of convection within the circulation of the vortex and the impact of this convection on the structure and evolution of the vortex are investigated. A conceptual model is presented to explain how convective redevelopment within the MCV causes low-level heights to fall and cyclonic vorticity to grow downward to the surface. Applying this conceptual model to a tropical marine environment is also considered.

1. Introduction

The formation and structure of midlevel cyclonic circulations within the stratiform region of some mesoscale convective systems (MCSs), particularly mesoscale convective complexes [MCCs; defined in Maddox (1980a)], has received considerable attention in recent years (e.g., Leary and Rappaport 1987; Brandes 1990; Bartels and Maddox 1991). These circulations, also known as mesoscale convective vortices (MCVs), are warm cored in the middle and upper troposphere and cold cored in the lower troposphere and near the tropopause (Zhang and Fritsch 1987; Menard and Fritsch 1989; Johnson and Bartels 1992). First identified by Johnston (1981), MCVs rely upon diabatic heating for their formation. Cyclonic vorticity is typically maximized in the midlevels, while anticylonic vorticity, associated with the lower-tropospheric cold pool, prevails at the surface.

A unique characteristic of MCVs is the possible role they may play in tropical cyclogenesis (Bosart and Sanders 1981; Velasco and Fritsch 1987; Miller and Fritsch 1991; Zehr 1992; Laing and Fritsch 1993a,b; Fritsch et al. 1994; Harr et al. 1996; Bister and Emanuel 1997; Ritchie and Holland 1997; Simpson et al. 1997). For example, Bosart and Sanders (1981) noted that the system that caused the Johnstown, Pennsylvania, flood of July 1977 had associated with it a cyclonic circulation of substantial intensity in the lower and middle troposphere, and that once this system moved over the Atlantic Ocean, the cyclonic circulation was observed at the surface, where it developed to tropical storm intensity. Velasco and Fritsch (1987), in their study of MCCs in both North and South America, found that during a two-year period there were at least five cases where an MCC (with its associated MCV) was a direct precursor

Corresponding author address: Dr. Robert F. Rogers, NOAA/AOML Hurricane Research Division, 4301 Rickenbacker Causeway, Miami, FL 33149.
E-mail: rogers@aoml.noaa.gov

to tropical cyclogenesis. Laing and Fritsch (1993a,b), in their satellite climatologies of MCCs over the Indian monsoon region and Africa, noted several instances in both locations where MCCs later developed into tropical depressions after they moved over water. Harr et al. (1996), Ritchie and Holland (1997), and Simpson et al. (1997) all studied tropical cyclogenesis in the western Pacific using satellite imagery and aircraft data. They found that interactions between MCVs and larger-scale cyclonic circulations as well as among several MCVs played important roles in modulating tropical cyclogenesis.

Understanding the role MCVs may play in tropical cyclogenesis is made difficult by the fact that while the primary organizational features that mark the onset of genesis require cyclonic vorticity to exist at the surface, cyclonic vorticity within MCVs is often confined to the midtroposphere. Therefore, an important question to ask when considering how MCVs may lead to tropical cyclogenesis involves understanding how cyclonic vorticity develops in the lower troposphere, especially at the surface.

Bister and Emanuel (1997) have proposed that downward motion within the mesoscale downdrafts of a convective system can serve to transport midlevel vorticity to the surface. In their idealized modeling studies of the genesis of Hurricane Guillermo, they found that sufficient precipitation (which in their model was provided by an essentially unlimited source of water in the upper troposphere) was needed to provide enough evaporation to drive the mesoscale downdraft to bring vorticity to the surface. For this mechanism to be operative, the source layer for the convection must be above the region of subsidence (e.g., overrunning convection). Using a three-dimensional quasigeostrophic model, Montgomery and Enagonio (1998) show that peripheral low-level positive potential vorticity, used to parameterize convection in their model, wraps into the main cyclonic circulation under the midlevel vortex, producing a vertically stacked vortex in the mid- to lower troposphere.

Other approaches to addressing the question of low-level vortex amplification have operated in the framework of potential vorticity. These approaches invoke the concept of the Rossby–Burger–Prandtl penetration depth (Hoskins et al. 1985; Shapiro and Montgomery 1993), which indicates the vertical extent of the fields of stability (mass field) and vorticity (momentum field) perturbations that produce a potential vorticity (PV) anomaly. Examples of studies that have incorporated this concept include analytical studies by Ritchie and Holland (1997), who found that increasing the horizontal scale of a PV anomaly through vortex merger and increasing the background vorticity within which merger occurs both increased the penetration depth of their anomaly. Fritsch et al. (1994) studied the effects of successive cycles of convection on the strength of a midlevel PV anomaly and the horizontal extent of the vorticity associated with the PV anomaly. They investigated a case where an MCS over Colorado formed an MCV, as deduced from examining satellite imagery and tracking radar echoes. During the next 3 days, the vortex moved across the central United States and was instrumental in initiating and organizing five successive MCSs. After each cycle of convection, the horizontal extent of the vortex was observed to increase, nearly tripling its initial diameter over its 3-day life cycle. Furthermore, composite analyses revealed that the magnitude of the midlevel PV anomaly increased. For several of the convective cycles, convection was observed to develop *within* the cyclonic circulation of the vortex, a crucial factor in explaining its amplification. They speculated that the increase in the amplitude of the midlevel PV anomaly would increase the penetration depth of the vortex, possibly leading to surface cyclogenesis.

In the study presented here, the Pennsylvania State University–National Center for Atmospheric Research (Penn State–NCAR) fifth-generation Mesoscale Model (MM5; Anthes and Warner 1978; Grell et al. 1994) is used to simulate the long-lived MCV described in Fritsch et al. (1994, hereafter F94), with the goal of understanding how convective regeneration within the existing midlevel cyclonic circulation leads to the development of a cyclonic circulation at the surface. The use of a fully nonlinear, primitive equation numerical model to study processes important in tropical cylcogenesis is not new (e.g., Tuleya and Kurihara 1981; Zhang and Bao 1996; Liu et al. 1997; Farfan and Zehnder 1997); however, relatively little has been done to specifically address the impact of multiple convective redevelopments on the structure of an existing MCV. While the MCV studied here occurred over land, it is assumed that the insights into how convective redevelopment affects the structure of an MCV can be extended to warm-core vortices over the tropical oceans (to be discussed in a later section).

Section 2 describes the characteristics of the numerical model used in the experiment. Section 3 presents a brief description of the case under investigation, while section 4 shows the results of the simulation, including a comparison with a cloud-scale-resolution simulation of the third convective cycle. Section 5 introduces a conceptual model of the impact of convective redevelopment on the structure of an existing MCV. A summary and concluding remarks are presented in section 6.

2. Description of model

MM5 is a nonhydrostatic model that uses the terrain-following vertical coordinate σ. In this study, the domain configuration consists of two meshes: an outer mesh with a grid length of 54 km and a two-way interactive inner mesh with a grid length of 18 km (Fig. 1). The number of grid points for the (x, y, σ) dimensions of the coarse and fine meshes are (65, 64, 29) and (100, 88, 29), respectively. The spacing between sigma levels is smallest ($\approx$5 mb) in the lower troposphere to

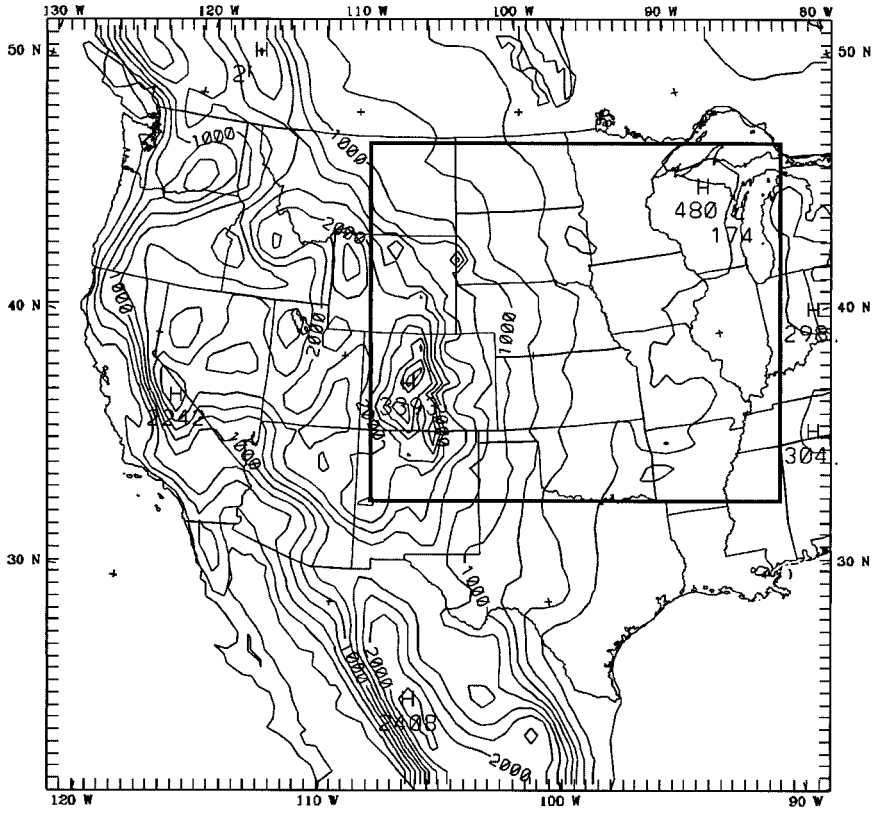

FIG. 1. Coarse-mesh domain (Δx = 54 km) and plot of coarse mesh terrain. Contour interval is 250 m. Bold line indicates position of fine-mesh domain (Δx = 18 km).

resolve the boundary layer processes better and increases with increasing elevation to a maximum spacing of about 50 mb. The model is statically initialized at 0000 UTC 15 July 1982, and a 48-h simulation is performed.

Precipitation processes on the grid scale are represented with an explicit moisture scheme that includes predictive equations for cloud water, cloud ice, rain, and snow (Dudhia 1989; Zhang 1989). A high-resolution planetary boundary layer (PBL) parameterization (Zhang and Anthes 1982) is used to simulate the vertical mixing of temperature, water vapor, momentum, and cloud water. The parameterization uses a surface energy budget that is based on the force–restore method developed by Blackadar (1979). This budget is dependent on the surface sensible and latent heat fluxes, substrate fluxes, and radiative fluxes. The radiative fluxes are determined by a scheme that accounts for the effects of water vapor and cloud cover (Benjamin and Carlson 1986), while the surface heat and moisture fluxes are computed from similarity theory. To represent deep, moist convection in the model, the Kain–Fritsch (KF) parameterization scheme is used on both meshes (Kain and Fritsch 1990, 1993). This scheme employs a relatively sophisticated mass-flux cloud model to determine entrainment and detrainment rates as a function of the local (grid element) environment, and it includes the effects of moist downdrafts.

Several modifications to the various components of the modeling system were implemented to more realistically account for the warm-season weak-flow convective environment encountered by the model. One significant modification involves a form of dynamic initialization using the convective parameterization scheme. Specifically, radar data are used as a source for initiating and suppressing convection in the model using the KF scheme. The methodology (Rogers et al., 2000) involves digitizing radar reflectivity to the model grid at high temporal frequencies (e.g., every 15 min). In regions or times where there are no radar data available, the convective parameterization is allowed to operate independently. If the radar indicates there is no convection present (convection being defined when reflectivity values exceed a threshold value), the parameterization scheme is not allowed to initiate convection. If radar indicates convection is present but the parameterization is not going to initiate it, then convection is forced within the scheme. In the simulation presented here, radar nudging is used for the first 24 h of the simulation. Other modifications are described in the appendix.

The Barnes (1964) objective analysis routine was used on the model output in some of the figures in this study. The routine consisted of running a bandpass filter (Maddox 1980b) that isolates wavelengths on the me-

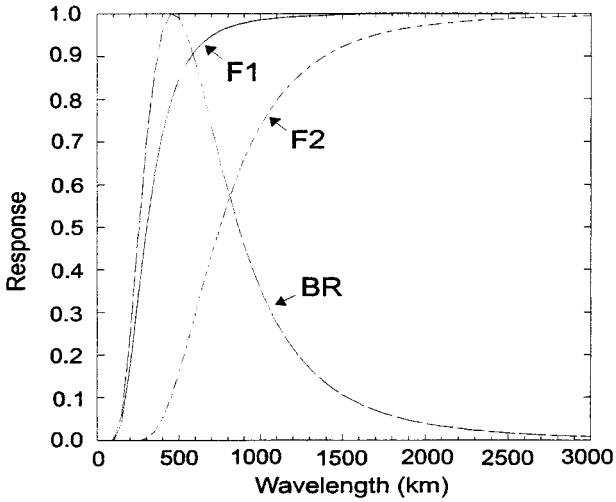

FIG. 2. Response functions for bandpass filter. The filter indicated by curve F1 allows almost all wavelengths greater than 500 km to pass through untouched, while nearly eliminating wavelengths less than 200 km. The filter indicated by curve F2 allows wavelengths greater than 1500 km to pass almost entirely and wavelengths from 500 to 1500 km in varying degrees, while completely eliminating wavelengths less than 500 km. The difference between the two filters, curve BR, results in a bandpass that isolates wavelengths between 300 and 700 km.

soscale while filtering smaller and larger-scale features. This filter, shown in Fig. 2, maximizes the response of features having wavelengths between 300 and 700 km. This was the typical diameter of many of the features associated with the convective systems, such as the low-level cold pool, mesohigh, and midlevel cyclonic circulation (Fritsch et al. 1994).

3. Description of case

The case selected for simulation is the multiconvective-cycle system documented in F94. As mentioned in the introduction, this case exhibited a midlevel mesovortex and an amplifying midlevel PV anomaly as it tracked eastward across the central United States and underwent five successive cycles of convective development and decay. The present study focuses on the first three cycles, especially the third cycle wherein a particularly intense cycle of convective redevelopment occurred. A brief summary is provided here. More detailed analysis and discussion is available in F94.

a. Synoptic setting

At 0000 UTC 15 July 1982, the synoptic-scale environment over much of the United States was dominated by a large cyclonic disturbance centered over southwestern Canada and a broad high pressure system anchored over the southeastern United States (Fig. 3). Between these two large-scale features the mid- to upper-level flow was generally westerly and weak with speeds rarely exceeding 15 m s^{-1}, even at 200 mb (Figs. 3a–d). Several short waves were propagating through the weak midtropospheric flow (Fig. 3b). Of particular note is a 500-mb cold anomaly, indicative of relatively lower static stability, covering much of the high plains. This cold anomaly corresponded well with the region into which several MCSs that had formed along the east slopes of the Rocky Mountains were propagating. Pronounced veering, indicative of strong warm advection in the surface to 700-mb layer (Figs. 3c and 3e), dominated the region beneath the midlevel cold anomaly and helped to further reduce the static stability. From the surface to about the 850-mb level, the flow was predominately southerly with a well-defined low-level jet (LLJ) transporting high-θ_e air northward to the MCSs.

b. Evolution of mesoscale features

The first cycle of convection had its roots in the daytime heating that occurred over the Front Range of the Rocky Mountains. Convection drifted eastward and formed a mesoscale convective system covering much of northeastern Colorado and western Nebraska by 0000 UTC 15 July (Figs. 4a,b). During the next 3 h, the system developed a nearly circular, contiguous cold cloud shield. A surface mesoanalysis a few hours later (not shown) revealed a mesohigh and cold pool, with an anticyclonic wind pattern, over much of northwestern Kansas and eastern Colorado. The system propagated steadily eastward overnight and weakened. Since the axis of the LLJ also shifted eastward and rotated clockwise overnight (not shown), the vortex-bearing MCS remained on the western fringe of the jet and never intercepted the highest-θ_e air. By midmorning, however, the system was encroaching into the moist ribbon and a second convective cycle followed (Figs. 4c–e). A surface mesohigh was again evident under the convective system (Fig. 5a), with evidence of a weak wake low or trough developing at the back edge of the system. The 850-mb environment (Fig. 5b) at this time shows that the surface-based outflow boundary lay directly in the path of the LLJ transporting high-θ_e air. Moreover, the cycle was beginning at a time when the LLJ typically strengthens, suggesting that another outbreak of convection was imminent.

Only a few hours after the second convective cycle dissipated, a third cycle began over central Iowa (Fig. 6). Contrary to conventional wisdom (e.g., Purdom 1976), the location of the new convection was well behind the now-weakening line of storms along the eastern outflow boundary and well north of the trailing edge of the cold outflow (cf. Figs. 5a and 6a). By 0600 UTC, a well-developed MCC was apparent over central and eastern Iowa (Fig. 6b). As is typical of MCCs, the system began to weaken toward morning, and by 1200 UTC 16 July most of the deep convection had dissipated. By the end of this convective cycle, the mesohigh increased

in amplitude and areal extent compared to 12 h earlier (cf. Figs. 5a and 7). The amplitude of the surface mesotrough, evident after the previous convective cycle, also increased.

Radar echo traces performed in F94 (Fig. 8) show a cyclonic circulation associated with each cycle of convection. The diameter of the cyclonic circulations is likely to be an underestimate since it is unlikely that precipitation would extend all the way to the fringes of the circulation. A qualitative comparison of the diameter of the closed circulation indicated by the echo traces shows that the diameter of the circulation approximately triples between 0000 UTC 15 July and 1200 UTC 16 July (i.e., from about 50 to 150 km). Furthermore, computations of midlevel potential vorticity (not shown; see F94 for a complete discussion) show that the magnitude of the PV maximum nearly doubles between 15 and 17 July. These observations show that the vortex increases both in horizontal scale and intensity. Concurrent with this strengthening are several cycles of convective activity, with each outbreak of convection occurring coincident (or very nearly so) with the MCV itself. How these convective outbreaks strengthen the MCV and whether such outbreaks cause cyclonic vorticity to penetrate closer to the surface are the subjects of the next section.

4. Simulation results

a. Vortex track and intensity

Analyses of midlevel vorticity for the 48 h of simulation time show that the model is reasonably successful at capturing the track of the vortex. Figure 9 shows the locations of the vortex at 12-h intervals for both the observations and the simulation. During the first 24 h (commencing 0000 UTC 15 Jul) the modeled track of the vortex closely follows the observed track. This is not surprising, since it is during this time period that parameterized convection is prescribed by radar data. After the first 24 h, the modeled vortex turns sharply to the north-northeast until 1200 UTC 16 July, at which point it follows a track similar to that of the observed vortex, although it is now displaced about 200 km to the north.

Amplification of the simulated vortex occurs during time periods that correspond well with the grid-resolved[1] precipitation that develops with, and as a consequence of, each convective cycle. For example, Fig. 10 compares the temporal evolution of the midlevel potential vorticity (following the vortex) to the grid-resolved precipitation. It is clear that the magnitude of the PV increases following each convective cycle and that the time of the peaks in PV lags the peaks in precipitation by about 4–8 h. During the first two convective cycles, when the grid-resolved precipitation rates within the circulation are comparable, the PV undergoes a cycle of intensification and subsequent decay as the rainfall diminishes. During the third cycle, the rainfall rates increase sharply. The PV also increases sharply, reaching a value nearly 1.5 times the peak value that occurred during the first convective cycle. The increase in midlevel PV is qualitatively similar to the observed increases for this case (cf. Fig. 10; F94). Moreover, similar relationships between vortex genesis and grid-resolved rainfall have been found in other numerical studies of warm-season convective events (e.g., Zhang and Fritsch 1987).

b. Convective cycles

Fields of the simulated 1-h parameterized and grid-resolved rainfall and midlevel bandpass-filtered wind vectors and vorticity for the 36-h simulation (Fig. 11) show that the model is successful at reproducing the evolution of the vortex and the development of convection within the vortex. Based upon the wind vectors and vorticity values, it is clear that the model was successful in creating a midlevel vortex in roughly the same location as was observed (cf. Figs. 11a and 9). Both parameterized and grid-resolved rainfall are associated with the vortex and much of the precipitation is occurring within the cyclonic circulation. Midlevel vorticity within the vortex is quite high, with values exceeding $30 \times 10^{-5}\ s^{-1}$ at 0600 UTC. By the time of the beginning of the second cycle of convection (1500 UTC 15 Jul), the vortex had drifted eastward along the Nebraska–Kansas border. In contrast to the first convective cycle, the precipitation in the early stages of this cycle is located primarily on the eastern side of the cyclonic circulation, forming an arc-shaped pattern that is roughly consistent with observations (cf. Figs. 4c and 11b). During the next 6 h, parameterized convection (still prescribed by the radar-nudging scheme) and resolvable-scale condensation continue to occur within the cyclonic circulation. The spatial distribution of the convection and resolvable-scale condensation appears chaotic and highly asymmetrical with respect to the vortex center. At times, the vorticity maximum weakens and a new center forms in a location slightly displaced from the location of the previous center but well within the overall circulation of the vortex. For example, notice that the vorticity maximum in Figs. 11b–d alternately shifts southeastward and then northeastward as the overall vortex circulation travels generally eastward. Notice also the weak vorticity center (labeled A) that is ''spun off'' from the main circulation. Each of the vorticity

[1] When discussing mesoscale model results (i.e., grid lengths between 10 and 30 km), care should be taken in equating *parameterized* heating/rainfall with *convective* heating/rainfall and *grid-resolved* heating/rainfall with *stratiform* heating/rainfall, since in many simulations, including this one, grid-resolved heating is at least marginally ''convective.'' The implications of this lack of a clear scale separation are discussed in a later section detailing a high-resolution simulation.

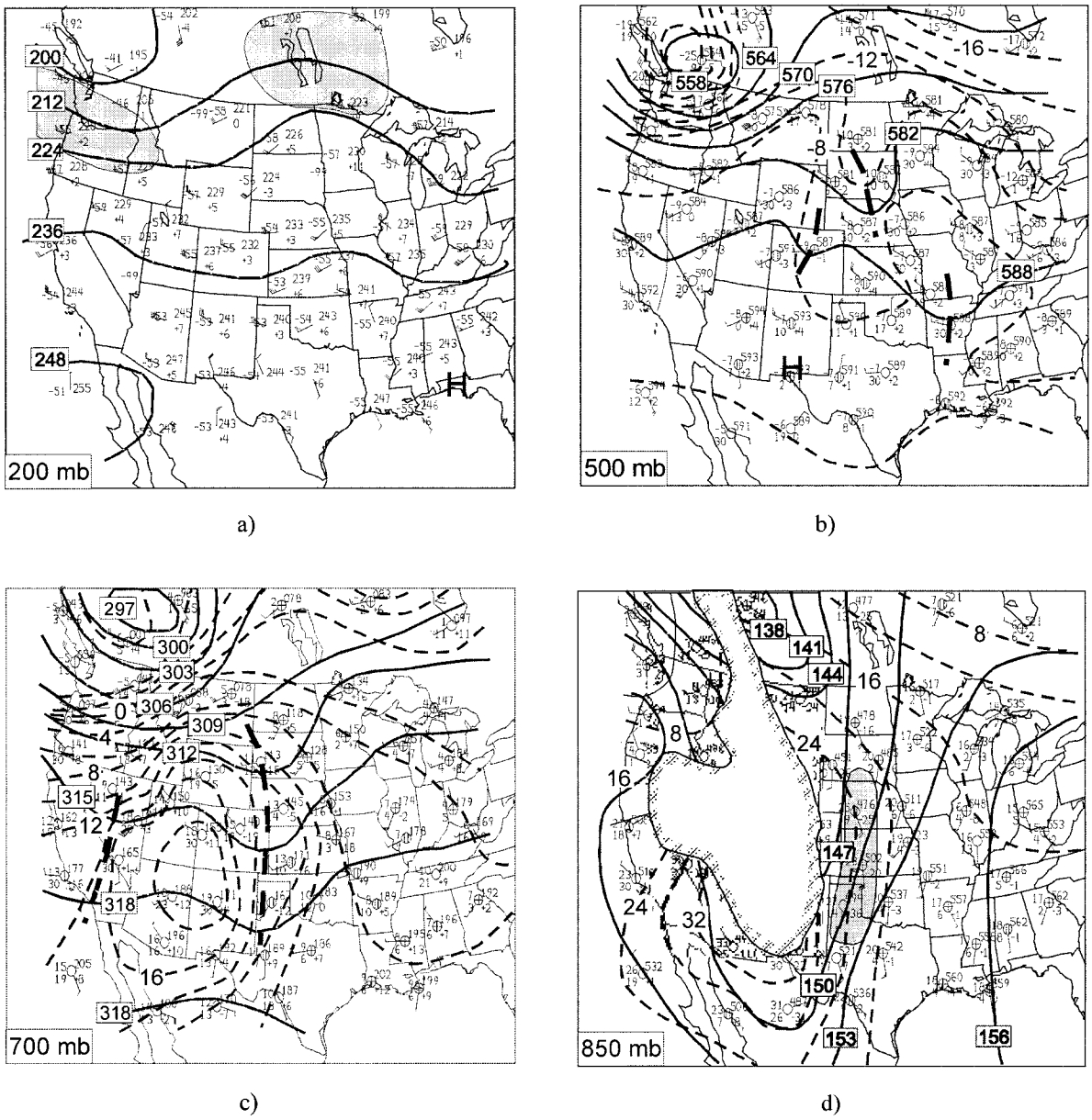

FIG. 3. Synoptic-scale analyses at 0000 UTC 15 Jul 1982. Wind barbs are in m s^{-1} for all plots. Full barb = 5 m s^{-1}; flag = 25 m s^{-1}. (a) The 200-mb geopotential height; contour interval 120 m. Shaded region denotes areas where winds $\geq$ 25 m s^{-1}; (b) 500-mb geopotential height (solid, contour interval 60 m) and temperature (dashed, contour interval 2°C). Thick dashed lines denote locations of short-wave troughs; (c) same as (b) but for 700-mb geopotential height, contour interval 30 m; (d) 850-mb geopotential height (solid, contour interval 30 m) and temperature (dashed, contour interval 4°C). Partial-hatched region over western United States denotes locations above 850 mb. Light shaded region denotes areas where the winds $\geq$ 12.5 m s^{-1}. (e) Surface analysis of sea level pressure with a contour interval of 4 mb.

centers follows a different life cycle: some centers merge and strengthen while others shear off from the main system and dissipate. Similar life cycles have been found in observations of pretropical depression cloud clusters over the tropical oceans (P. Black 1997, personal communication). Toward the end of the second cycle, the arc-shaped system consolidates, and by 0000 UTC 16 July an elongated vortex, with an average diameter of approximately 150 km, is readily evident in the wind vector and vorticity fields (Fig. 11d).

Shortly after the second convective cycle terminates, parameterized convection begins again in the model. By 0300 UTC 16 July, convection covers much of western Iowa (Fig. 11e), with scattered areas of weak grid-resolved rainfall ($<$0.1 cm h^{-1}) embedded within the parameterized rainfall region. Except for a small area of

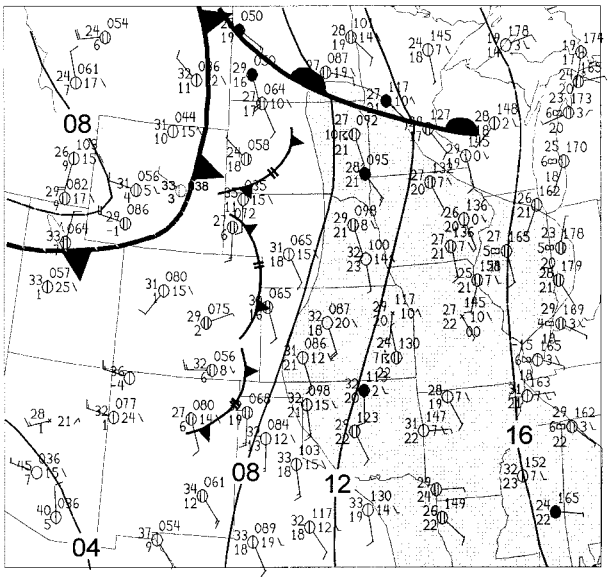

e)

FIG. 3. (*Continued*) Shaded region denotes areas where the dewpoint is greater than or equal to 20°C. Outflow boundary symbols infer the approximate locations of mesoscale convective systems as deduced from satellite and radar imagery in conjunction with surface data.

spurious parameterized convection near south-central Nebraska, most of the parameterized convection is located well within the cyclonic circulation and is consistent with observations (cf. Figs. 11e and 6). The midlevel vorticity associated with the vortex exhibits two axes at 0300 UTC. The one extending to the southeast reflects the earlier vorticity maximum that propagated northeastward from Kansas while the one extending to the west, in the northwestern part of the rainfall shield, is a new feature just starting to develop. During the next few hours, this new vorticity maximum intensifies to values that are about double that of the previous maximum and, as a result, the western axis emerges as the dominant feature of the vortex. The period of intensification of the vortex corresponds with the time when the area of grid-resolved rainfall expands into the center of the vortex circulation. It also corresponds to the period when the resolvable-scale rainfall rates intensify strongly (maximum rain rates increase from less than 1 cm h^{-1} to greater than 5 cm h^{-1}).

In addition to the precipitation and midlevel vorticity fields, the model also reproduces well the low-level pressure, temperature, and wind fields associated with the convective cycles. Figure 12 shows conditions in the lower troposphere prior to the development of the third convective cycle (i.e., 0000 UTC 16 Jul). A strong southwesterly LLJ, with wind speeds exceeding 15 m s^{-1}, is evident. This LLJ is similar to what was observed (cf. Figs. 5b and 12a) and what has been found to accompany other MCC events (Maddox 1983; Cotton et al. 1989). Extremely high values of θ_e accompany the jet, with some values approaching 355 K in the 850–700-mb layer. As indicated in Fig. 12a, the outflow boundary from the second convective cycle is oriented nearly perpendicular to the axis of the LLJ. It provides lifting of high-θ_e air as the southwesterly flow encounters the mesoscale cold dome. Cross sections of bandpass-filtered potential temperature, winds, vorticity, vertical motions, and unfiltered equivalent potential temperature are taken along a cross section parallel to the low-level jet and across the outflow boundary (Figs. 12b,c). The surface-based cold anomaly (centered at point L) extends upward to approximately 850 mb. Above this level, a weaker cold anomaly (centered at point M) straddles the crest of the mesoscale ascent over the surface-based cold pool. Yet a third center of anomalously cold air (point N) appears in the zone of maximum mesoscale descent. Inspection of the temperature tendencies in each of these three centers of anomalously cold air indicates that they formed through different processes. In particular, the cold pool centered at point L is primarily the result of the cooling from parameterized penetrative moist downdrafts. In contrast, the cooling centered on point M results from adiabatic expansion and in-cloud melting. The third region of maximum cooling (centered around point N) is the result of strong subcloud-layer evaporation of resolvable-scale precipitation. Together, these processes produce a broad and deep mesoscale cold dome. Immediately above the cold dome is a warm anomaly, indicating that there is a layer of locally higher stability centered around the 500-mb level. While the location of the relative vorticity maximum is lower than the level of maximum stability, the potential vorticity maximum (not shown) coincides with the high-stability layer, indicating that the potential vorticity had significant contributions from the stability term, consistent with the analysis of F94. Profiles of θ_e taken over southwestern Iowa between 0000 and 0400 UTC 16 July (Fig. 12d) show that rapid destabilization is occurring. Values of θ_e in the lower troposphere increase markedly during this time, with increases as large as 10 K occurring at 800 mb. The rapid destabilization (as a consequence of the low-level jet overrunning the surface-based cold pool) closely resembles the destabilization mechanism that occurred during the developmental period of the MCS documented by Trier and Parsons (1993).

Figure 13 shows surface pressure analyses taken after the second and third convective cycles. After the second convective cycle (0000 UTC 16 Jul) there is a mesoscale cold pool with a divergent anticyclonic outflow beneath the vortex and a generally east–west outflow boundary in northeastern Kansas and northern Missouri, in agreement with observations (cf. Figs. 5a and 13a). Notice that the midlevel mesoscale cyclonic circulation center (point C in Fig. 11d) lies directly above the surface-based cold pool and associated mesoscale *ridge*. After the third cycle (1200 UTC 16 Jul), a pronounced pres-

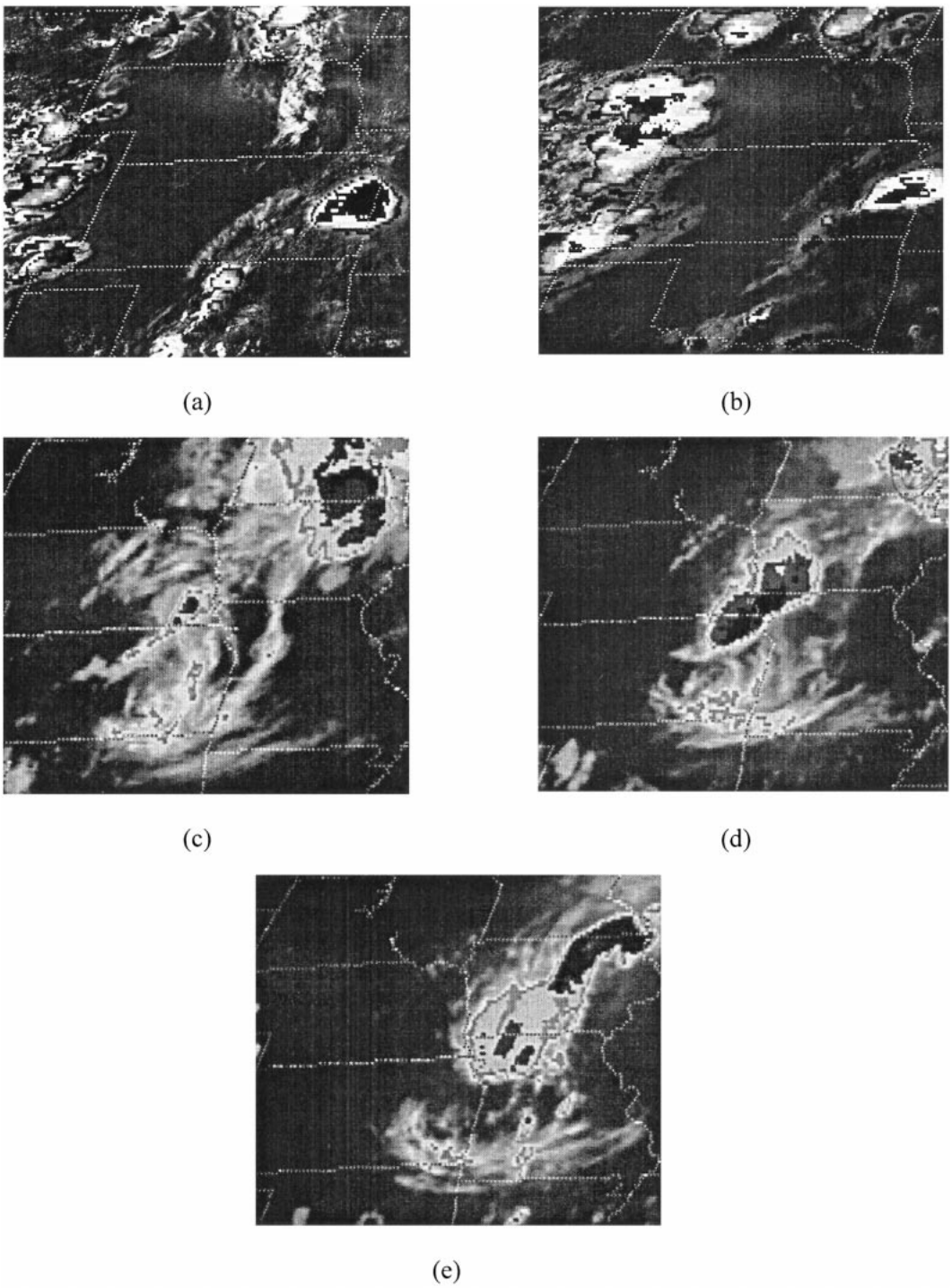

FIG. 4. Enhanced infrared satellite imagery valid at (a) 2131 UTC 14 Jul, (b) 0001 UTC 15 Jul, (c) 1502 UTC 15 Jul, (d) 1801 UTC 15 Jul, and (e) 2101 UTC 15 Jul 1982.

sure *trough* is located directly under the midlevel vortex, consistent with what was observed at this time (cf. Figs. 5b and 13b). This pressure trough persists even though the surface-based cold pool associated with the convective system remains beneath the center of the vortex.

c. Vortex amplification diagnostics

Since radar data were used to prescribe parameterized convection for the first 24 h, the model is free to develop features without any outside intervention only during

the second 24-h period, when the intense MCC occurred. Changes in the vertical structure of the vortex focus on this latter time period. Cross sections are used to illustrate changes in the vertical distribution of diabatic heating, winds, relative vorticity, equivalent potential temperature, relative humidity, and geopotential height[2] and virtual temperature anomalies at 0300 and 0900 UTC 16 July. In order to capture the salient mesoscale features and minimize variations caused by smaller-scale transient features such as parameterized convection at individual grid elements, multiple cross sections are averaged. The locations of these cross sections are shown in Fig. 11e. Five cross sections, scanning a swath approximately 100 km wide, are taken in a southwest–northeast orientation, along the path of the vortex during this time.

At 0300 UTC, parameterized convection is occurring nearly 150 km behind (north of) the outflow boundary leftover from the previous convective cycle (Fig. 14a), while weak grid-resolved heating is located in the lower troposphere within the region of parameterized convection (Fig. 14c; grid-resolved heating appears in areas with less than 100% relative humidity because of the averaging of several cross sections). Strong resolvable-scale moistening tendencies have caused the air underneath the convection to become nearly saturated, with relative humidity values over 80% in the lower troposphere. By 0900 UTC, diabatic heating associated with the system has intensified significantly. Parameterized convective heating remains fairly weak (Fig. 14b), but grid-resolved heating has intensified to greater than 25 K h^{-1} at midlevels (Fig. 14d). The area of strong heating (>10 K h^{-1}) spans almost the entire troposphere, extending from about 800 mb to the 250-mb level. An area of diabatic cooling dominates the lower troposphere in the rear (northeast) of the convective system.

Cross sections of geopotential height anomaly, θ_e; relative vorticity; and virtual temperature anomaly (Fig. 15) show the evolution of the vortex structure during the convective redevelopment cycle. At 0300 UTC a negative height anomaly is evident in the midtroposphere, collocated with a region of parameterized convection (cf. Fig. 14a), while positive anomalies exist in the upper troposphere and at the surface. The vortex is clearly shown to be confined to the midlevels (Fig. 15c), while anticyclonic flow is evident aloft and at the surface. Convective initiation occurs as a ribbon of low-level high-θ_e air is transported in a strong jet that encounters the cold pool left from the previous convective cycle (Fig. 15a). Virtual temperature anomalies are positive in the upper troposphere, with the maximum anomaly approaching 2.5°C at 250 mb, while negative values predominate above 200 mb and at the surface (Fig. 15c). By 0900 UTC, the vortex has amplified considerably. The midlevel negative height anomaly has strengthened,

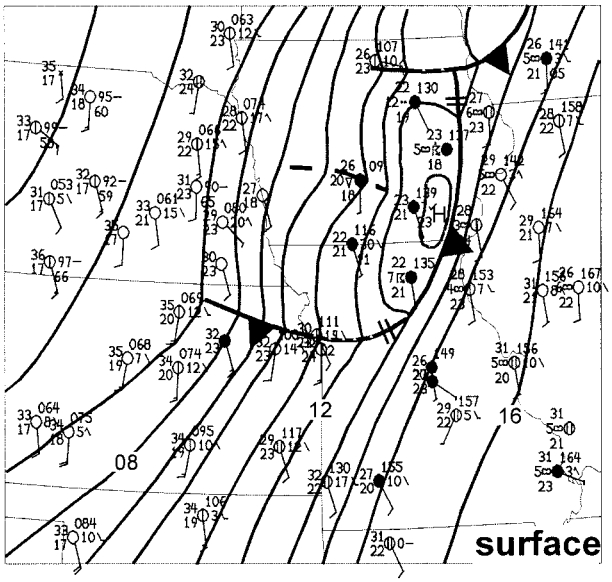

(a)

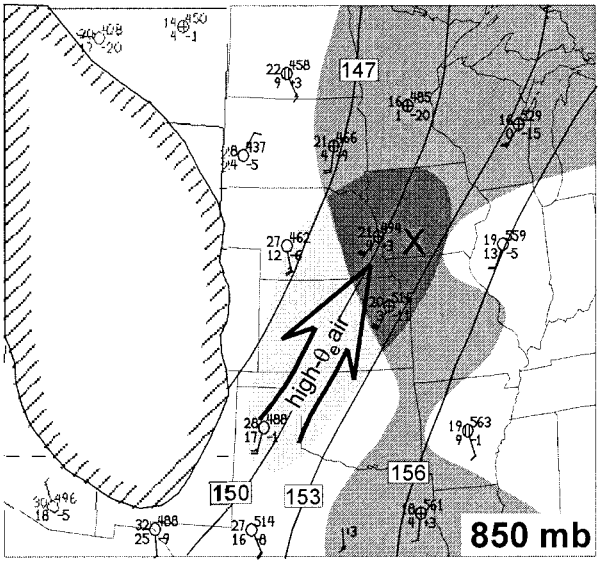

(b)

FIG. 5. (a) Surface mesoanalysis valid at 0000 UTC 16 Jul 1982; (b) 850-mb geopotential height (solid, contour interval 30 m) valid at 0000 UTC 16 Jul 1982. Large × indicates the location of the midlevel mesovortex. Light shading denotes areas where wind speed ≥ 12.5 m s^{-1}, dark shading denotes areas where dewpoint depression <5°C.

[2] While geopotential height is not explicitly computed in the model, but rather in a postprocessing program, a comparison of bandpass-filtered height fields to bandpass-filtered pressure perturbation fields (p', not shown) shows that the location and amplitude of the height anomalies are directly correlated with the p' anomalies, indicating that interpretations of the height fields are reflective of processes explicitly occurring in the model.

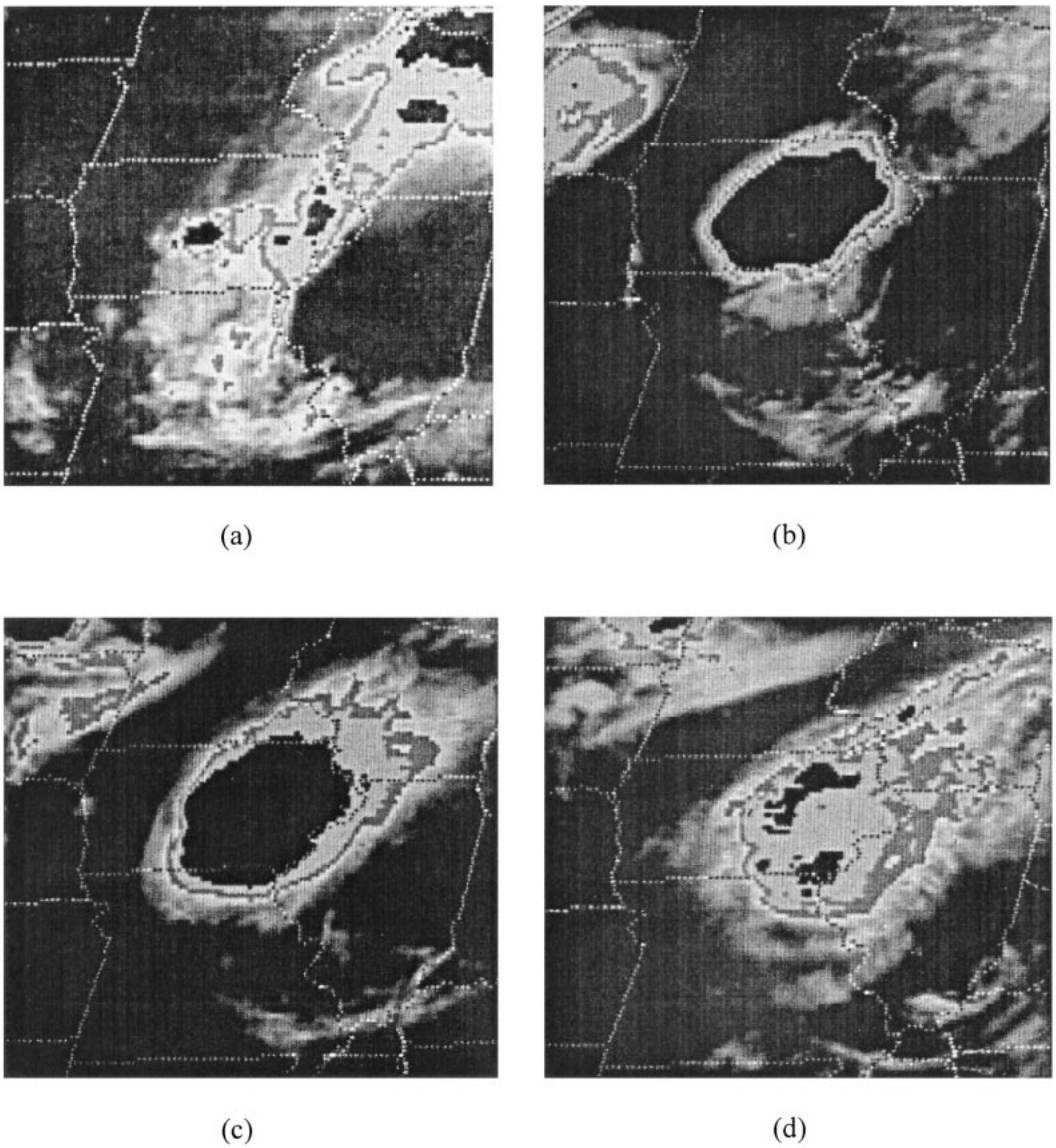

FIG. 6. Enhanced infrared satellite imagery valid at (a) 0231 UTC 16 Jul, (b) 0600 UTC 16 Jul, (c) 0900 UTC 16 Jul, and (d) 1201 UTC 16 Jul 1982.

and negative anomalies are now evident at the surface (Fig. 15b). The θ_e field continues to show the inflow of high-θ_e air in the low levels, while the midlevel core is now nearly moist adiabatic, with a 12-K anomaly. Midlevel cyclonic vorticity has increased, *and it now penetrates down through a strong low-level negative virtual temperature anomaly and reaches the surface* (Fig. 15d). Above the vortex core, the positive virtual temperature anomaly has amplified to greater than 2.5°C over a broad area.

Time–height series of virtual temperature anomaly, bandpass-filtered geopotential height, relative vorticity, sea level pressure perturbation, and temperature and vorticity budgets following the vortex from 0300 to 1200 UTC 16 July were computed (Fig. 16). The time–height series of virtual temperature anomaly (Fig. 16a) shows at 0300 UTC a structure that would be expected of a vortex confined to the midlevels: a weak virtual warm anomaly in the upper troposphere (between 0 and 0.5 K) overlying a virtual cold anomaly with a maximum amplitude of −1.5 K at the surface. During these first few hours only parameterized convection is occurring within the vortex. By 0530 UTC, however, grid-resolved heating begins, and shortly thereafter the amplitude of the virtual warm anomaly increases markedly, reaching a maximum of 2.5 K at 400 mb by 0900 UTC. At the same time the mid- and upper-level warm anomaly is amplifying, the low-level cold anomaly is deepening, so that by 1200 UTC it is nearly 300 mb deep. A time series of the sea level pressure perturbation (Fig. 16b),

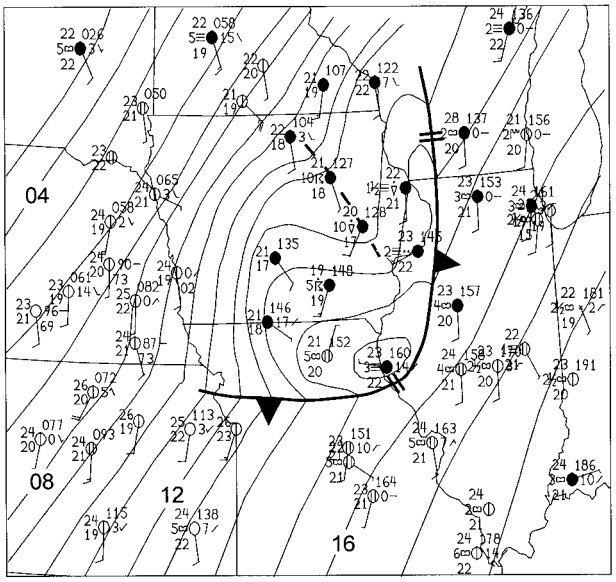

FIG. 7. Surface mesoanalysis valid at 1200 UTC 16 Jul 1982.

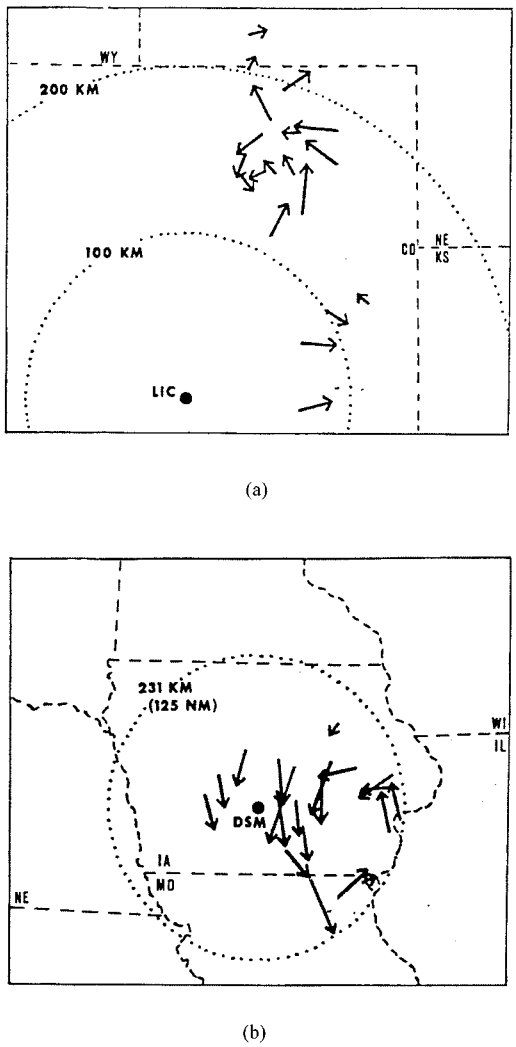

FIG. 8. Composite of radar echo movements for (a) 0000–0100 UTC 15 Jul and (b) 1100–1200 UTC 16 Jul 1982 (adapted from Fritsch et al. 1994).

computed as the difference between the pressure underneath the vortex and the mean of the mesoscale environment (i.e., a 250-km square box centered on the vortex), initially shows high pressure at the surface. As the virtual warm anomaly amplifies in the upper troposphere, the surface high pressure perturbation decreases, so that by 0700 UTC low pressure appears at the surface. This low pressure reaches its maximum strength at 0900 UTC, concurrent with the maximum amplitude of the virtual warming aloft. Since the surface pressure falls even as the surface-based cold layer strengthens and deepens, the surface pressure falls must be imposed externally, that is, from above. Evidently, the upper-level warming in this case becomes strong enough so that it hydrostatically overwhelms the relative high pressure anomaly associated with the surface-based cold pool underneath the convective system, thereby resulting in relative low pressure at the surface.

The effect of the virtual temperature anomaly on the height field is shown in a time–height series of band-pass-filtered geopotential height (Fig. 16c). Initially, the negative height anomalies are confined to the midlevels, just below the positive virtual temperature anomaly, and anomalously high heights exist near the surface and near 200 mb. Over the next 6 h, as grid-resolved heating begins, significant changes occur in these fields. In the midlevels, the height of the maximum negative anomaly descends and then, between 0600 and 0900 UTC, the magnitude increases sharply. Concurrently, the high heights near the surface diminish so that, shortly after 0600 UTC, negative height anomalies appear at the surface. (This is of course consistent with the trace of sea level pressure anomaly shown in Fig. 16b.) *The increases in negative height anomaly occur despite the fact that the low-level virtual cold anomaly strengthens and deepens*, indicating that the effects on the lower troposphere of the virtual warming aloft (i.e., lower heights) are overwhelming the effects of the virtual cooling in the lower troposphere. The time–height series for relative vorticity (Fig. 16d) shows that at the beginning of the third convective cycle (0300 UTC) cyclonic vorticity is confined to the 320–770-mb layer, while weakly anticyclonic flow exists in the upper and lower troposphere. During the next 3 h, the low-level anticyclonic vorticity disappears as cyclonic vorticity penetrates *downward*, through the virtually cold air (Fig. 16a), and reaches the surface just after 0600 UTC, remaining there for the next 10 h (not shown). The midlevel vortex reaches its maximum amplitude at 1000 UTC, just *after* the maximum virtual warming aloft (cf. Figs. 16a and 16d), after which time it begins to weaken.

To understand the physical processes important in creating the thermal patterns associated with the vortex,

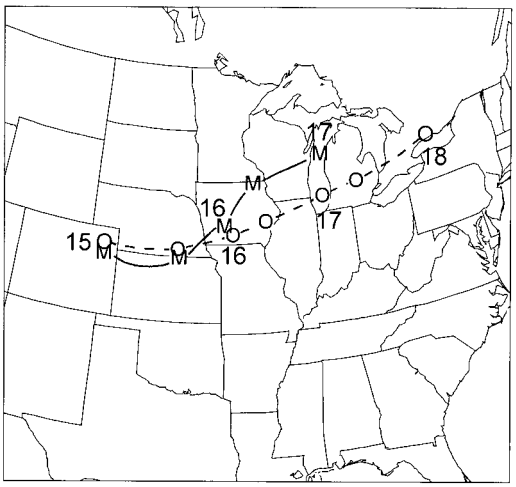

FIG. 9. Track and locations at 12-h intervals of observed vortex (dashed lines with O) and modeled 500-mb vorticity center (solid lines with M) starting at 0000 UTC 15 Jul.

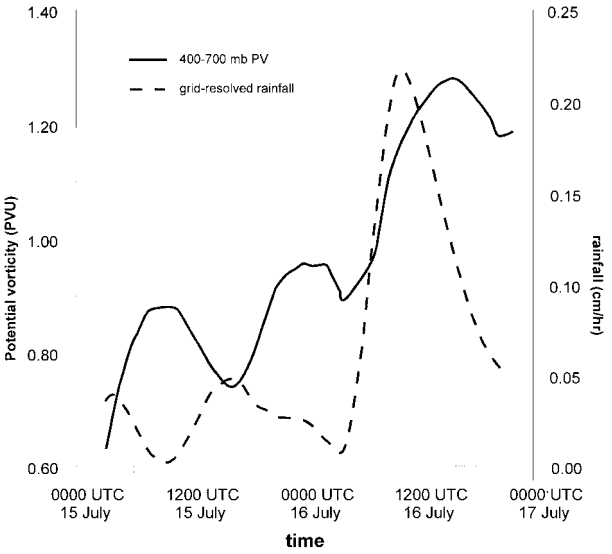

FIG. 10. Evolution of the simulated mean midlevel (400–700 mb) potential vorticity [solid, PVU ($\times 10^{-6}$ m^2 s^{-1} K kg^{-1})] and 1-h accumulated grid-resolved rainfall (dashed, cm) from 0000 UTC 15 Jul to 0000 UTC 17 Jul following the vortex. Values are areally averaged within a 250-km square box centered on the vortex, smoothed with a 5-h running mean.

a temperature budget following the vortex, from 0300 to 1200 UTC 16 July, was computed. The equation for temperature change in sigma coordinates may be written as follows:

$$\frac{\partial T}{\partial t} = -(\mathbf{V}_H - \mathbf{c}) \cdot \boldsymbol{\nabla}_H T - \dot{\sigma}\frac{\partial T}{\partial \sigma} - \frac{1}{\rho C_p}(\rho_0 g w) + F_{\text{conv}} + F_{\text{expl}} + F_{\text{diff}} + F_{\text{pbl}} + F_{\text{acou}}, \quad (1)$$

where $\mathbf{V}_H$ is the horizontal velocity, $\mathbf{c}$ is the motion of the vortex (5.1 m s^{-1} from 220°), w is the vertical velocity, $\dot{\sigma}$ is the vertical velocity in sigma coordinates, ρ_0 is the density of the reference state, and the constants g and C_p represent acceleration due to gravity and heat capacity at constant pressure of air, respectively. The first term on the right-hand side of Eq. (1) is the horizontal advection of temperature from flow relative to the system, the second term is the vertical advection, the third term is the temperature change due to adiabatic cooling or warming resulting from the vertical advection of the base-state pressure, and the terms F_{conv}, F_{expl}, F_{diff}, F_{pbl}, and F_{acou} are the temperature tendencies due to physical parameterizations of moist convection, grid-scale latent heat release, horizontal diffusion, planetary boundary layer processes (including vertical diffusion), and changes in pressure perturbation (an acoustical term), respectively. In the following figures, only the terms having first-order effects on the temperature tendency [horizontal advection, changes due to vertical motion (vertical advection plus adibatic effects), and parameterized and grid-resolved latent heating] are presented.

The time–height series of parameterized heating (Fig. 17a) shows a maximum contribution at 400 mb at 0500 UTC. While parameterized heating is occurring within the vortex from the start of the time series, it is not until several hours later that grid-resolved heating begins. The magnitude of the grid-resolved heating is considerably larger than that of the parameterized heating, and the level of maximum heating increases from 650 mb to nearly 400 mb by 1200 UTC. Horizontal advection (Fig. 17c) is fairly weak throughout the time series, while the contribution due to vertical motion (Fig. 17d) shows significant negative tendencies, representing strong upward motion that occurs at times closely corresponding to the grid-resolved diabatic heating. The total temperature tendency (Fig. 17e) shows little change in the midlevel temperature during the first few hours of the time series. The most significant change occurs in the midlevels between 0600 and 0900 UTC, where total tendencies in the 480–280-mb layer exceed 1.25 K h^{-1}. The timing of this maximum corresponds to the time when both parameterized and grid-resolved latent heating is occurring within the vortex. It represents the ''delicate difference'' (Tuleya and Kurihara 1981) between the parameterized and grid-resolved latent heat release and the cooling due to the vertical motion, resulting in a net warming during the period of rapid vortex amplification (see Fig. 16d).

A vorticity budget following the vortex was also computed for the time period from 0300 to 1200 UTC 16 July. The vorticity budget for frictionless flow in isobaric coordinates can be expressed as follows:

$$\frac{\partial \zeta}{\partial t} = -(\mathbf{V}_H - \mathbf{c}) \cdot \boldsymbol{\nabla}_H(\zeta + f) - \omega\frac{\partial \zeta}{\partial p} - (\zeta + f)\boldsymbol{\nabla}_H \cdot \mathbf{V}_H - \mathbf{k} \cdot \left(\frac{\partial \mathbf{V}_H}{\partial p} \times \boldsymbol{\nabla}\omega\right), \quad (2)$$

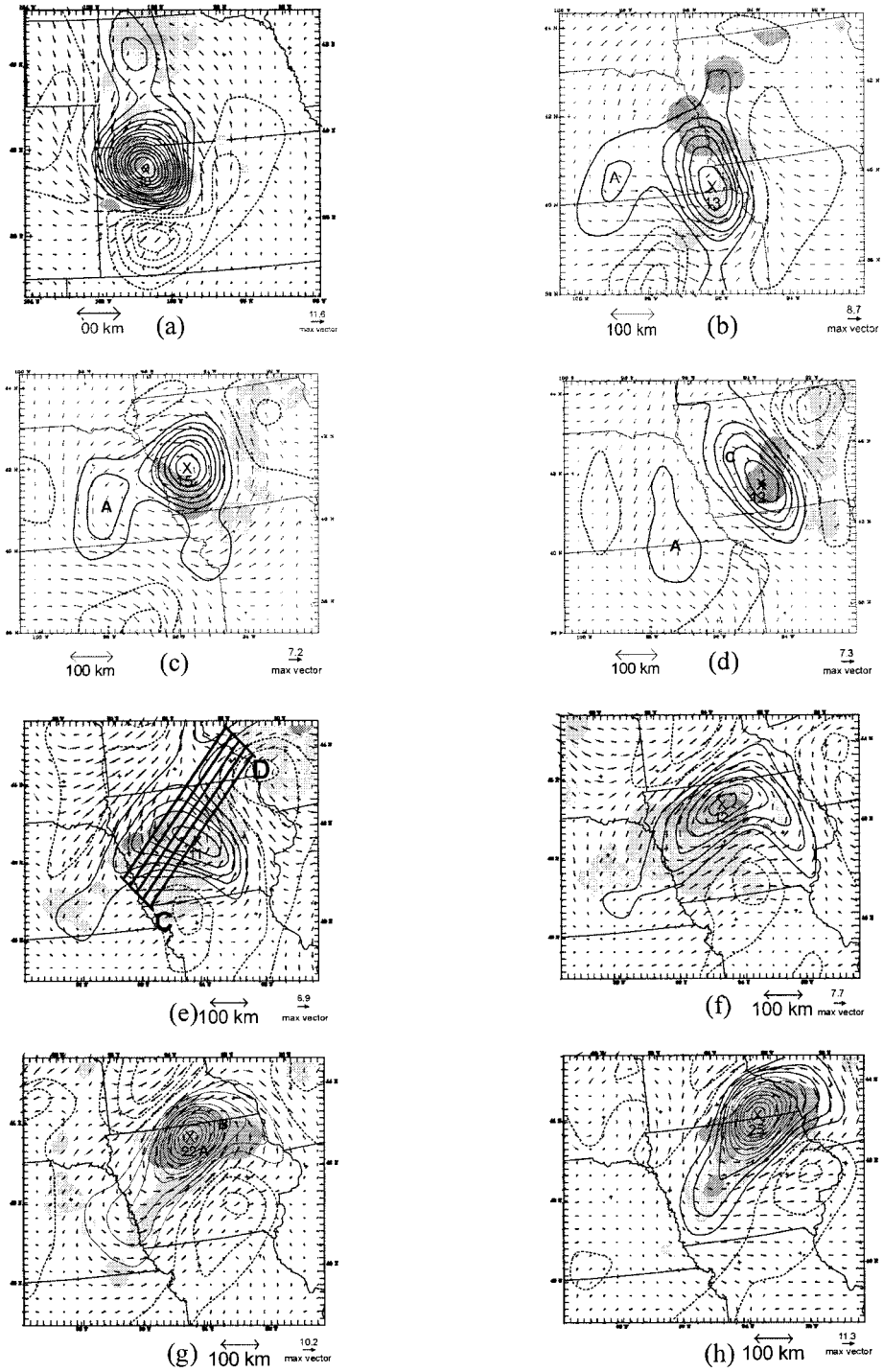

FIG. 11. Simulated hourly parameterized rainfall (light shading) and grid-resolved rainfall (dark shading) and bandpass-filtered wind vectors and relative vorticity [solid (negative) lines positive (negative), contour interval 2×10^{-5} s^{-1}] at the $\sigma = 0.5$ level. Locations of vorticity maxima are denoted with a $\times$: (a) 0600, (b) 1800, (c) 2100 UTC 15 Jul, (d) 0000, (e) 0300, (f) 0600, (g) 0900, and (h) 1200 UTC 16 Jul. Letter C in (d) denotes location of midlevel circulation center; A in (b)–(d) indicates transient vorticity center "spun off" from main circulation. Bold solid lines in (e) denote location of cross sections used in computing averages in Figs. 14 and 15. The A and B in (g) indicate locations of soundings in Fig. 27.

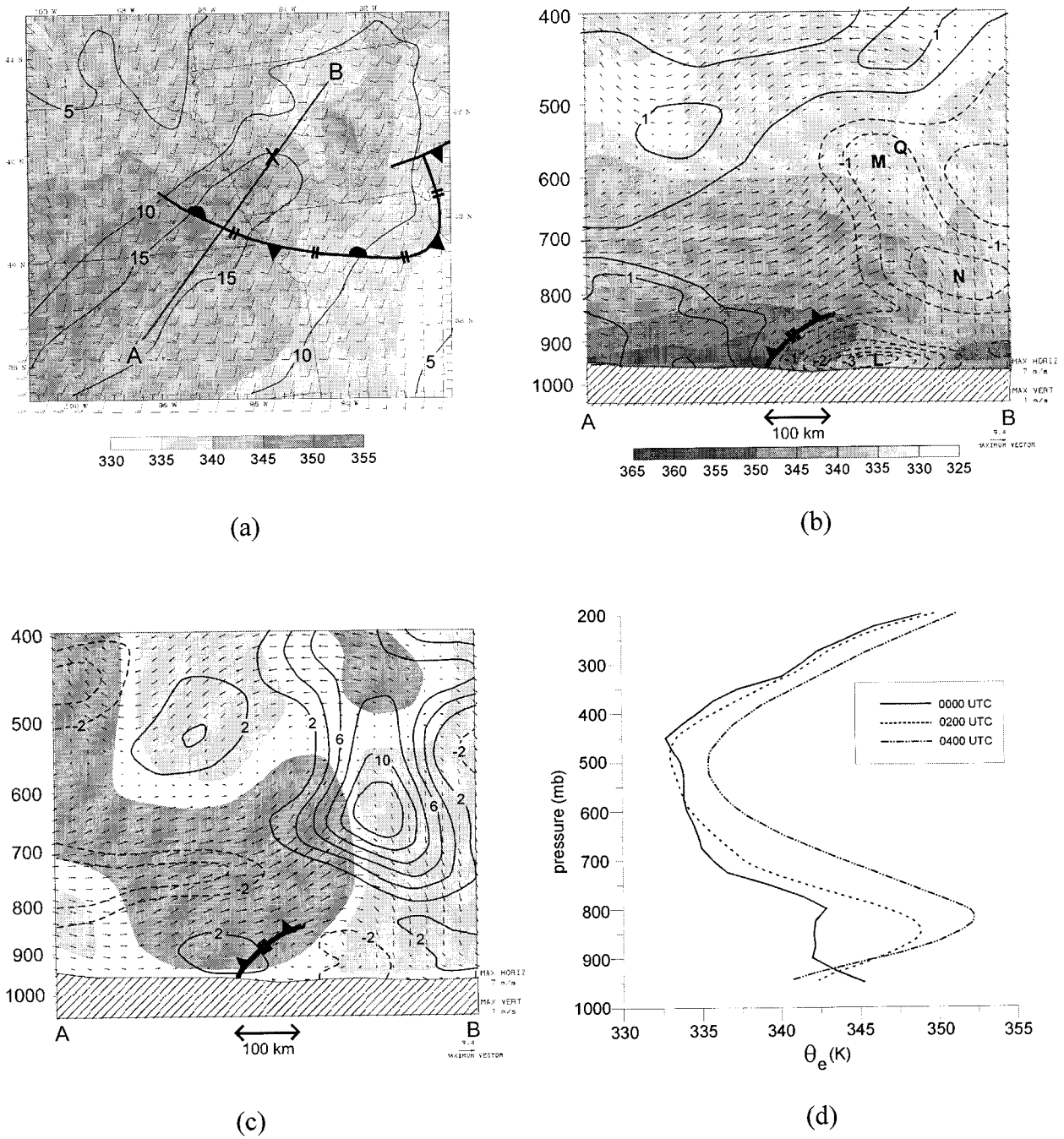

FIG. 12. (a) Simulated mass-weighted vertically averaged winds (solid, m s^{-1}; full barb = 10 m s^{-1}) and θ_e (K, shaded) in the 850–700-mb layer at 0000 UTC 16 Jul. Line AB and letter X denote locations of cross section and profiles in (b)–(d). Surface outflow boundary is superposed. (b) Cross section along line AB of simulated bandpass-filtered potential temperature (K), wind vectors in the plane of the cross section, and unfiltered equivalent potential temperature (K, shaded) at 0000 UTC 16 Jul. (c) Cross section of bandpass-filtered relative vorticity ($\times 10^{-5}$ s^{-1}), wind vectors in the plane of the cross section, and vertical motion (m s^{-1}, shaded). Dark (light) shading denotes upward (downward) motion. Point Q indicates the location of the maximum PV. Points L, M, and N are discussed in the text. (d) Vertical profile of θ_e at 0000, 0200, and 0400 UTC 16 Jul at point X from (a).

where ζ is the vertical component of relative vorticity, f the Coriolis parameter, $\mathbf{V}_H$ the horizontal velocity, $\mathbf{c}$ is the motion of the vortex, and ω the vertical velocity in isobaric coordinates. The first term on the right-hand side of Eq. (2) is the change in relative vorticity due to horizontal advection from flow relative to the system, the second term is the change due to vertical advection, the third term is the change due to stretching (divergence

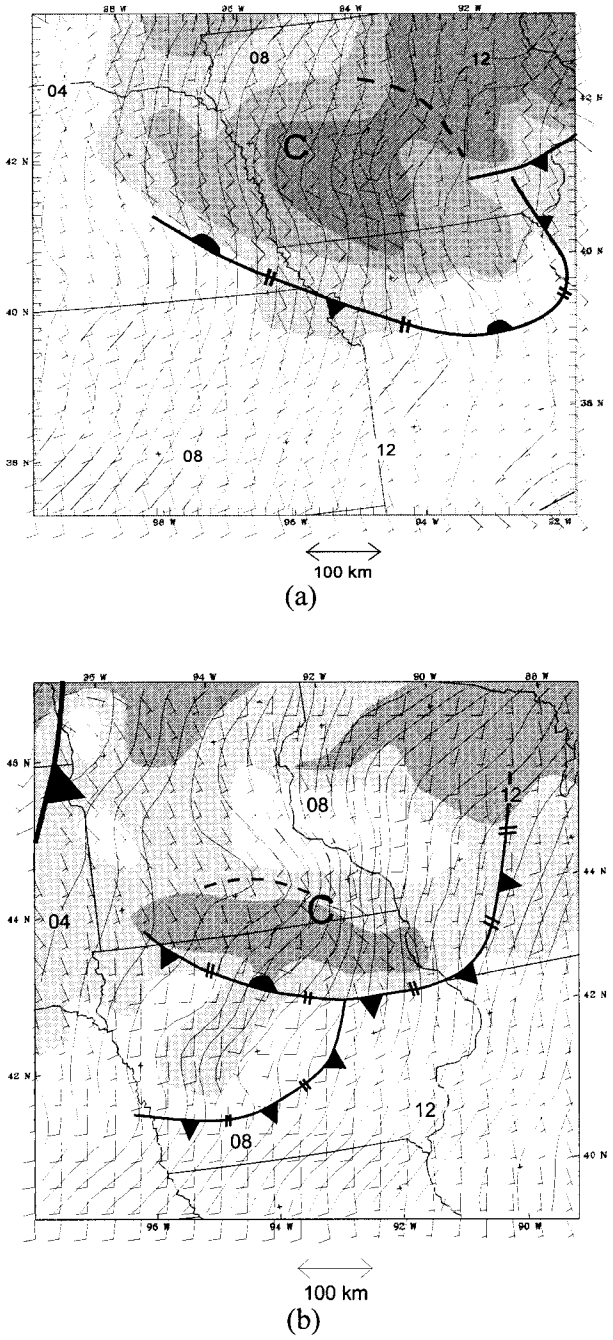

FIG. 13. Simulated sea level pressure (contour, 1 mb contour interval), wind barbs (m s^{-1}), and temperature (shading) at the $\sigma = 0.997$ level for (a) 0000 and (b) 1200 UTC 16 Jul. Letter C in both figures denotes location of midlevel circulation center (see Figs. 11d and 11h). Light, medium, and dark shading in (a) indicates areas less than 30°, 28°, and 26°C, while light and medium shading in (b) indicates areas less than 22.5° and 21.5°C.

or convergence), and the fourth term is the change due to tilting of horizontal vorticity into the vertical.

Figure 18 shows the terms in the vorticity equation given in Eq. (2). Horizontal advection of vorticity (Fig. 18a) is fairly weak during most of the time period. The vertical advection term shows strong negative tendencies in the layer below 500 mb and significant positive tendencies in the layer above 500 mb, especially during the time when grid-resolved heating is occurring. This is typical of a pattern of strong upward motion in the presence of a midlevel vorticity maximum. The main contributor to increasing vorticity in the mid- to lower troposphere is the stretching term. Maximum contributions occur at approximately 650 mb at 0900 UTC, coincident with the time of the maximum in grid-resolved heating and positive virtual temperature anomaly, while in the upper troposphere negative tendencies dominate. The tilting term shows a significant contribution to increasing midlevel vorticity in the early stages of the grid-resolved heating (i.e., 0500–0800 UTC). This contribution likely arises from the interaction of the upward motion with the strong vertical shear at the top of the low-level jet. The total vorticity tendency at the vortex center (Fig. 18e) shows that little change in the amplitude of the vortex occurs during the first few hours, the time when only parameterized convection is occurring within the vortex center. Substantial amplification occurs in the lower troposphere starting at around 0600 UTC, with the maximum amplification at 700 mb. This amplification continues to increase for the next few hours, so that by 0900 UTC vorticity increases as large as 2250×10^{-10} s^{-2} are evident at 650 mb. Amplification rates of this magnitude would give increases in vorticity of 81×10^{-5} s^{-1} over a 1-h time period. After this period of strong intensification, the lower-tropospheric positive vorticity tendency weakens. In the upper troposphere, negative vorticity tendencies predominate.

d. High-resolution simulation

In examining the evolution of the vortex during the MCC cycle, it is clear that the most rapid amplification occurs during the periods of intense grid-resolved diabatic heating (cf. Figs. 14–18). Furthermore, during the mature stage of the MCC, the southwestern edge (leading edge relative to the low-level inflow) of the convective system, where most of the vortex amplification occurs, exhibits a resolvable-scale heating profile that is more indicative of a ''convective'' profile, with heating over most of the troposphere and a maximum in the upper troposphere, while the northeastern (trailing) edge exhibits more of a traditional ''stratiform'' profile, with a maximum in the midtroposphere and with a deep layer of cooling in the lower troposphere (see, e.g., Johnson 1984 and Figs. 14c,d). Since most of the rapid vortex amplification occurs where the grid-resolved heating exhibits a convective-type profile, it is logical to ask whether or not the development of such grid-resolved heating profiles is physically meaningful. Since there is no clear physical scale separation between parameterized and grid-resolved processes at these grid lengths (Weisman et al. 1997; Kain and Fritsch 1998), it is nec-

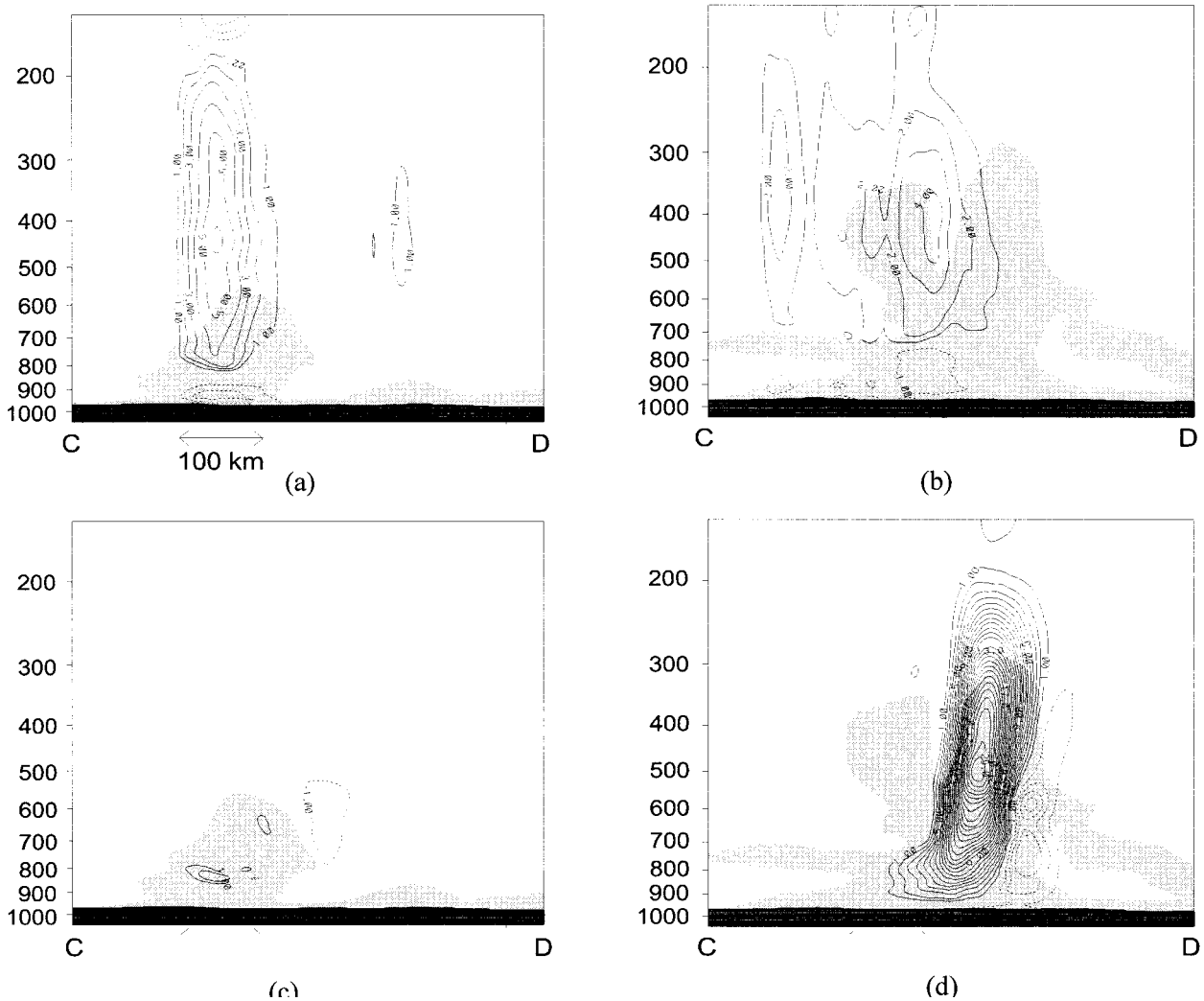

FIG. 14. Cross-sectional averages of parameterized heating (1 K h^{-1} contour interval) at (a) 0300 and (b) 0900 UTC 16 Jul, and grid-resolved heating (1 K h^{-1} contour interval) at (c) 0300 and (d) 0900 UTC 16 Jul. Shaded regions denote areas where relative humidity is greater than 80%.

essary to simulate this system using a much higher resolution. To accomplish this, the development period of the MCC cycle was simulated using a grid mesh with 2-km resolution. Grid lengths of this size fall well within the range of accepted resolutions for explicit simulations of intense convective systems (Weisman et al. 1997). By running a 2-km grid, there is no longer the problem of a fast-mode, parameterized convective overturning competing with a slowly evolving, grid-resolved component of the overturning.

Figure 19 shows the domains used in the 2-km simulation. The locations of the two innermost meshes were selected to capture the area at the tip of the low-level jet. This is the region where deep convection develops and becomes organized on the mesoscale during the first few hours of the third cycle and where the grid-resolved precipitation forms in the coarser-resolution run with parameterized convection. Using the output from the 18-km mesh, initial and boundary conditions were created for the time period from 0000 to 1200 UTC 16 July to run a 6-km mesh in a one-way nesting mode. This domain was integrated for 12 h, and the output from this run was used to create initial and boundary conditions for the 2-km mesh, which was integrated from 0000 to 0900 UTC in a one-way nesting mode.

As with the run with parameterized convection, the cloud-resolving simulation produced a broad shield of rainfall that stretched about 150 km across southwestern Iowa (not shown). Figure 20 shows the evolution of lower-tropospheric θ_e and cloud water during this time period. The low-level θ_e field shows the ribbon of high-θ_e air advancing from the south and southwest. As the areal extent and magnitude of the rainfall increases, the strength of the cold pool increases, so that by 0800 UTC a broad cold pool covers much of the domain, with a sharp boundary perpendicular to the low-level jet along

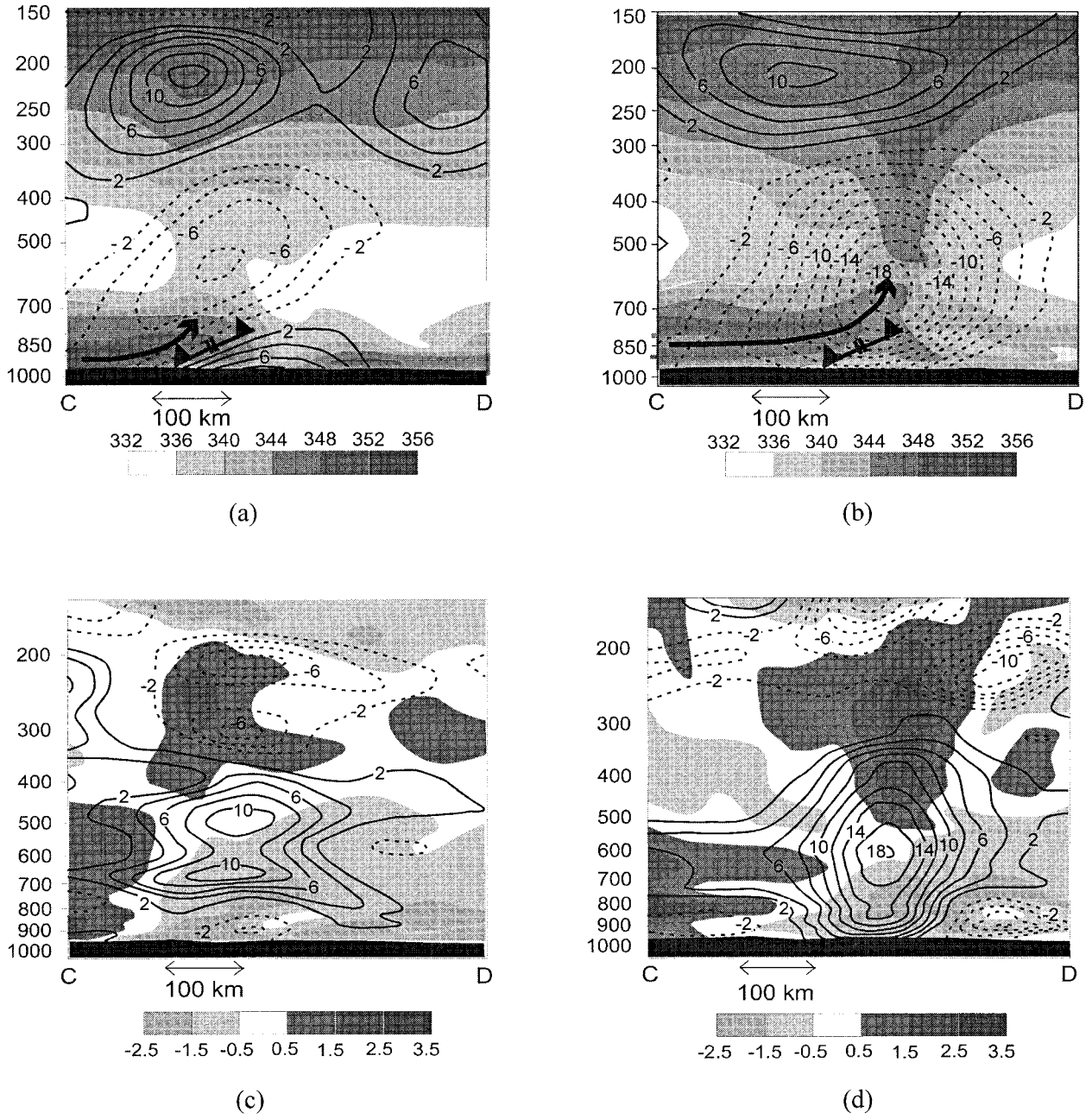

FIG. 15. Cross-sectional averages of bandpass-filtered geopotential height [2 m contour interval; solid (dashed) lines denote positive (negative) anomalies] and θ_e (K, shaded) at (a) 0300 and (b) 0900 UTC 16 Jul, and virtual temperature anomaly (°C, shaded) and bandpass-filtered relative vorticity (2×10^{-5} s^{-1} contour interval) at (c) 0300 and (d) 0900 UTC 16 Jul. Bold arrow in (a) and (b) follows streamlines of low-level inflow to convective system.

its southwestern edge. A contour outlining areas where cloud water >0.1 g kg^{-1} at the $\sigma = 0.7665$ level shows a ribbon of lower-tropospheric saturated air at 0200 UTC. As the rainfall shield expands and the cold pool strengthens, the areas of saturation undergo a change in organization, changing from a highly cellular pattern indicative of individual convective elements (0400 UTC) to a long contiguous swath, nearly 50 km wide at some points, extending along the edge of the cold pool (0800 UTC).

Associated with the strong cold pool and swath of saturated air at 0800 UTC is a zone of strong upward motion throughout the lower troposphere. Figure 21 shows vertical motion at selected levels in the lower troposphere. At the $\sigma = 0.952$ and 0.8775 levels, there is a solid swath of ascent greater than 0.5 m s^{-1} that

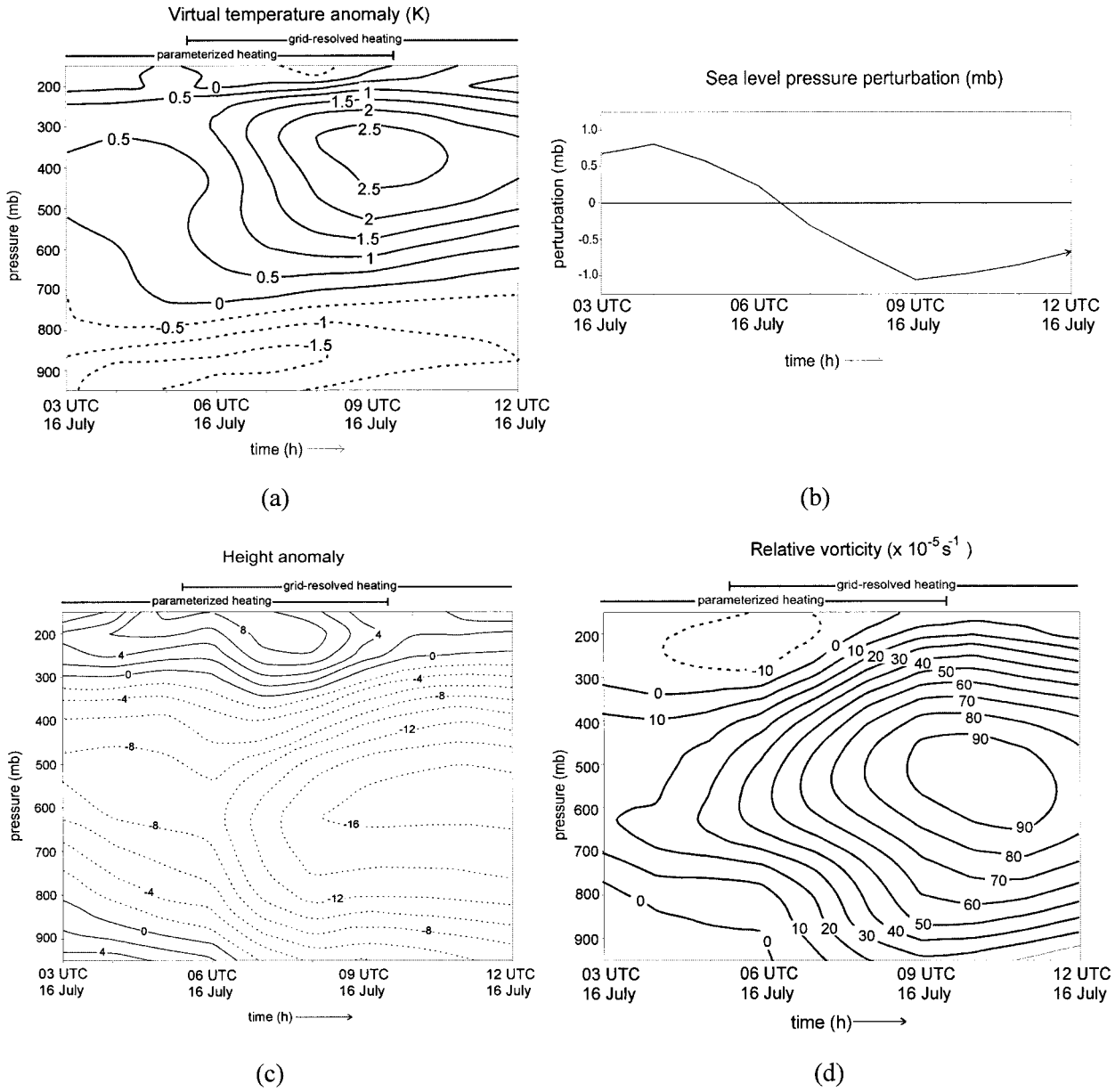

FIG. 16. (a) Vortex-following time–height series from 0300 to 1200 UTC 16 Jul of virtual temperature anomaly (K), (b) vortex-following time series of sea level pressure perturbation, (c) as in (a) but for bandpass-filtered geopotential height (m), and (d) as in (a) but for relative vorticity ($\times 10^{-5}$ s^{-1}). Times of parameterized and grid-resolved heating are indicated by arrows above (a), (c), and (d).

stretches for nearly 200 km. Behind this line (to the northeast) are scattered regions of both upward and downward motion, but within the line *all* the air is ascending. This feature is even more pronounced at the $\sigma = 0.7665$ level, where the swath of upward motion is wider, with even larger areas with upward motion exceeding 2 m s^{-1}. Such powerful ascent covering mesoscale areas produces large changes in the mesoscale environment. In particular, the upper-tropospheric warm anomaly generated by the previous convective cycles increases both in horizontal extent and magnitude (Fig. 22). By 0800 UTC, an area with θ_e values around 8 K larger than the ambient environment and covering over 100 km in average diameter is situated within the rainfall shield. By 0900 UTC, the rainfall pattern (Fig. 23) is characterized by a northwest–southeast-oriented line of heavy rainfall (>1–2 cm h^{-1}) along the southwest edge of the convective system (labeled convective) and a broad shield of generally light rainfall to the northeast, with a core of heavy rainfall in the middle of the shield (labeled stratiform). Embedded within this rainfall shield is a distinct cyclonic circulation in the midlevels.

A comparison of heating profiles taken from the 18- and 2-km simulations can help to understand whether

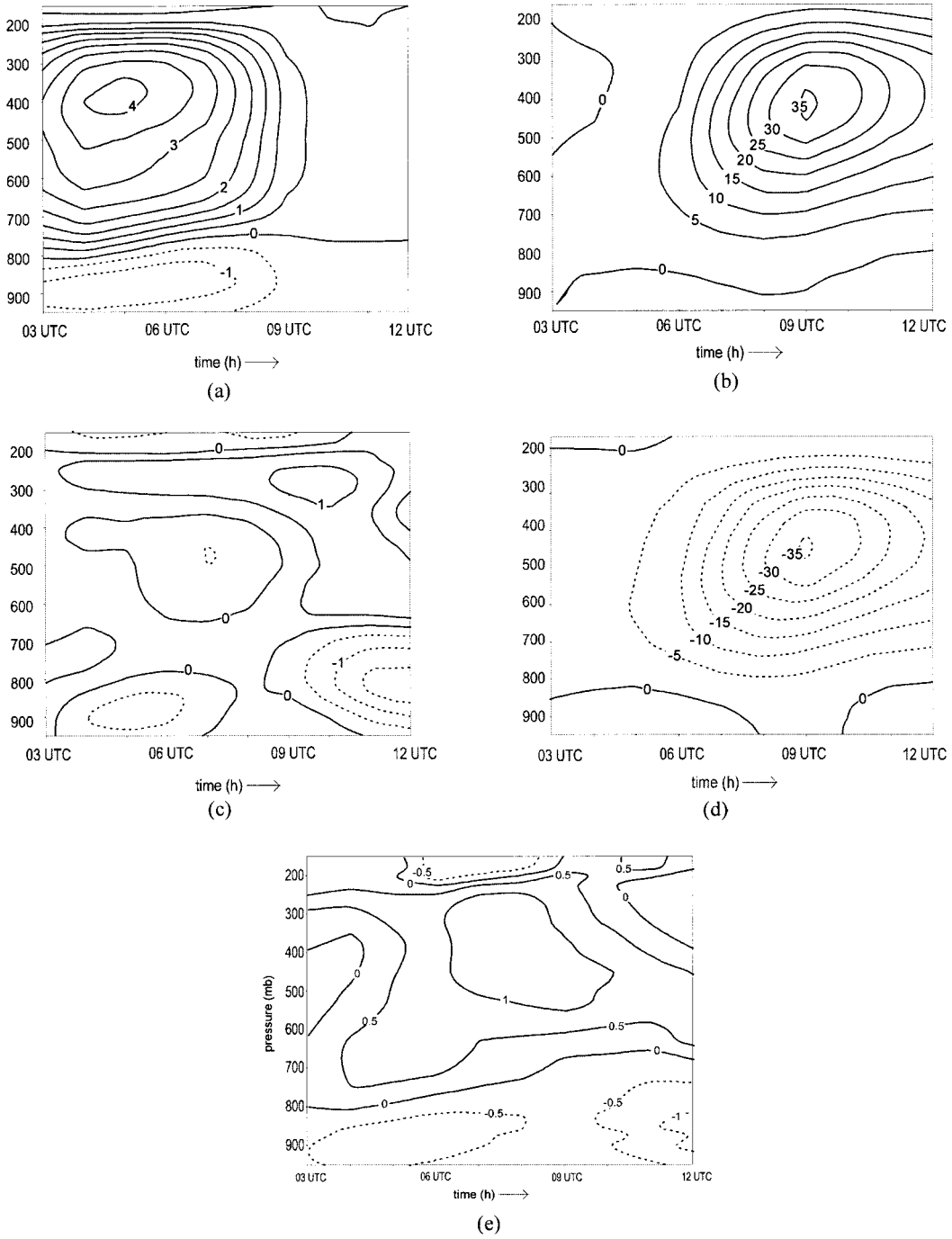

FIG. 17. Vortex-following time–height series from 0300 to 12 UTC 16 Jul for terms in temperature budget given in Eq. (1). Units are in K h^{-1} (note different contour intervals among figures). (a) Parameterized latent heat release, (b) grid-resolved latent heat release, (c) horizontal advection, (d) vertical motion, and (e) total temperature tendency.

the grid-resolved heating in the 18-km run is physically realistic. Figure 24a shows profiles at 0900 UTC of grid-resolved heating from all locations in the 18-km run where grid-resolved rainfall exceeded 0.1 cm h^{-1} and all locations within the ''stratiform'' region of the 2-km run where grid-resolved rainfall exceeded 0.1 cm h^{-1}. Significant differences are evident in the two profiles. The maximum heating in the 18-km run is stronger than the maximum heating in the 2-km run. Moreover, the vertical profile of heating in the 18-km run is more indicative of a convective-type heating profile, while the 2-km profile is more indicative of a stratiform-type

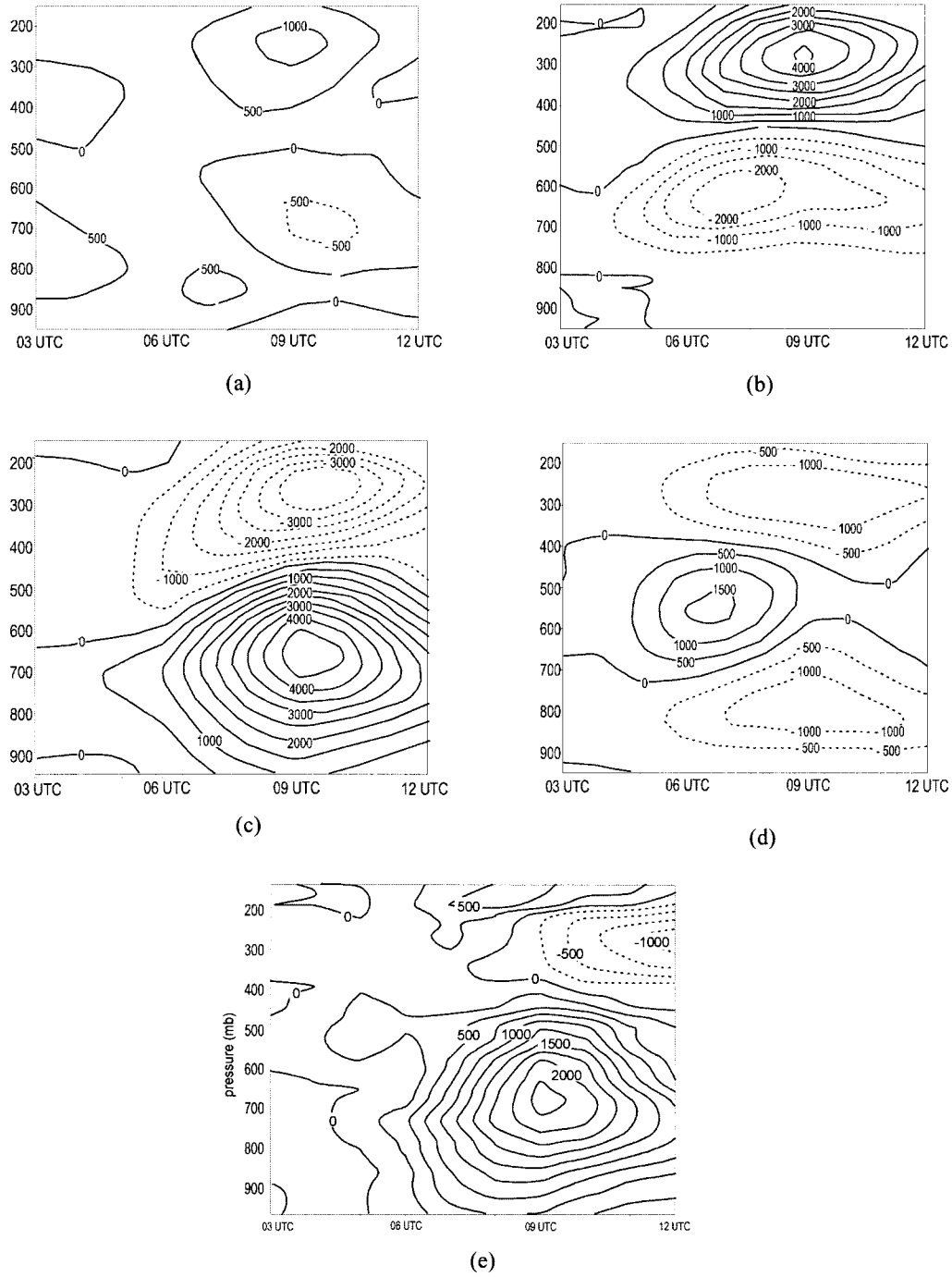

FIG. 18. Vortex-following time–height series from 0300 to 12 UTC 16 Jul for terms in vorticity budget given in Eq. (2). Units are $\times 10^{-10}$ s^{-2}. (a) Horizontal advection term, (b) vertical advection term, (c) stretching term, (d) tilting term, and (e) total vorticity tendency.

heating profile, with a deep layer of cooling beginning at around the melting level of 550 mb. Closer inspection of the 2-km results, though, shows that the heating that is associated with the heavy rainfall (and vortex production) exhibits a profile more closely characteristic of a convective-type profile. Figure 24b shows a separation of the profile from the 2-km run shown in Fig. 24a into profiles representing light (0.1 cm hr^{-1} $\leq$ rain rate $<$ 1 cm h^{-1}) and heavy (rain rate $\geq$ 1 cm h^{-1}) rainfall. From Fig. 24b it is evident that the profile from the

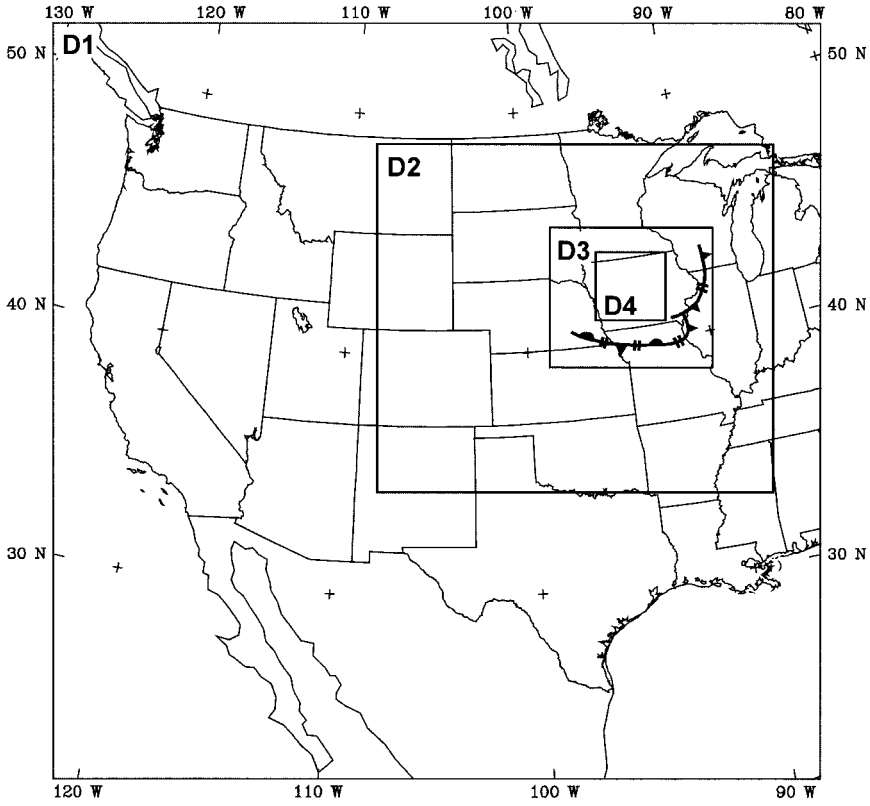

FIG. 19. Domains used in the 2-km simulation. Location of surface outflow boundary at 0000 UTC 16 Jul is superposed. Domain 3 (D3) has a grid length of 6 km; domain 4 (D4) has a grid length of 2 km.

heavy rainfall is very similar to a convective-type profile, and it is similar to the 18-km grid-resolved heating profile shown in Fig. 24a.

These results support the contention that the 18-km simulation with parameterized moist convection is reproducing a physically meaningful feature when its grid-resolvable moist ascent creates the mesoscale midlevel warm anomaly; that is, the midlevel warm-core mesovortex is not simply an artifact of deficiencies in the convective parameterization scheme. This suggests that intense heating rates, such as those that occurred during the vortex amplification of the MCC cycle here, can occur in nature, given sufficiently large destabilization rates. In the case simulated here, this destabilization occurs as a strong low-level jet transports high-θ_e air underneath the vortex. It is certainly possible, however, that the magnitude of the grid-resolved heating that results from this destabilization is larger in the 18-km simulation than what occurred in reality, since coarser-resolution simulations often take longer than their finer-resolution counterparts to develop the mesoscale features (e.g., a deep cold pool) that are important in facilitating continued destabilization and convective overturning (Weisman et al. 1997). Such a delay would allow for high-θ_e air to build up in the lower troposphere before convective overturning could occur, leading to stronger latent heat release once convection is initiated. Indeed, time series of rainfall amounts for the two simulations averaged over the area covered by the 2-km domain (not shown) show that area-averaged rainfall is greater in the 18-km simulation during the mature stages of the MCC by about 55%. Furthermore, since nonhydrostatic plumes would scale with the depth of the unstable layer, a 2-km simulation is only capable of resolving those plumes that represent the largest convective towers. It is possible that much of the turbulent mixing that would accompany rapid destabilization is accomplished by smaller-scale plumes that remain unresolved, implying that the depth and/or strength of the convectively unstable layers in the 2-km simulation are overestimated. Further research into the structure and mechanisms of buoyancy-driven turbulence, accompanied by simulations with higher horizontal and vertical resolution, would be necessary to investigate these issues.

5. Conceptual model

The results presented here illustrate how midlevel MCVs amplify and how their amplification can penetrate downward to the surface: The redevelopment of convection within an existing MCV increases the mag-

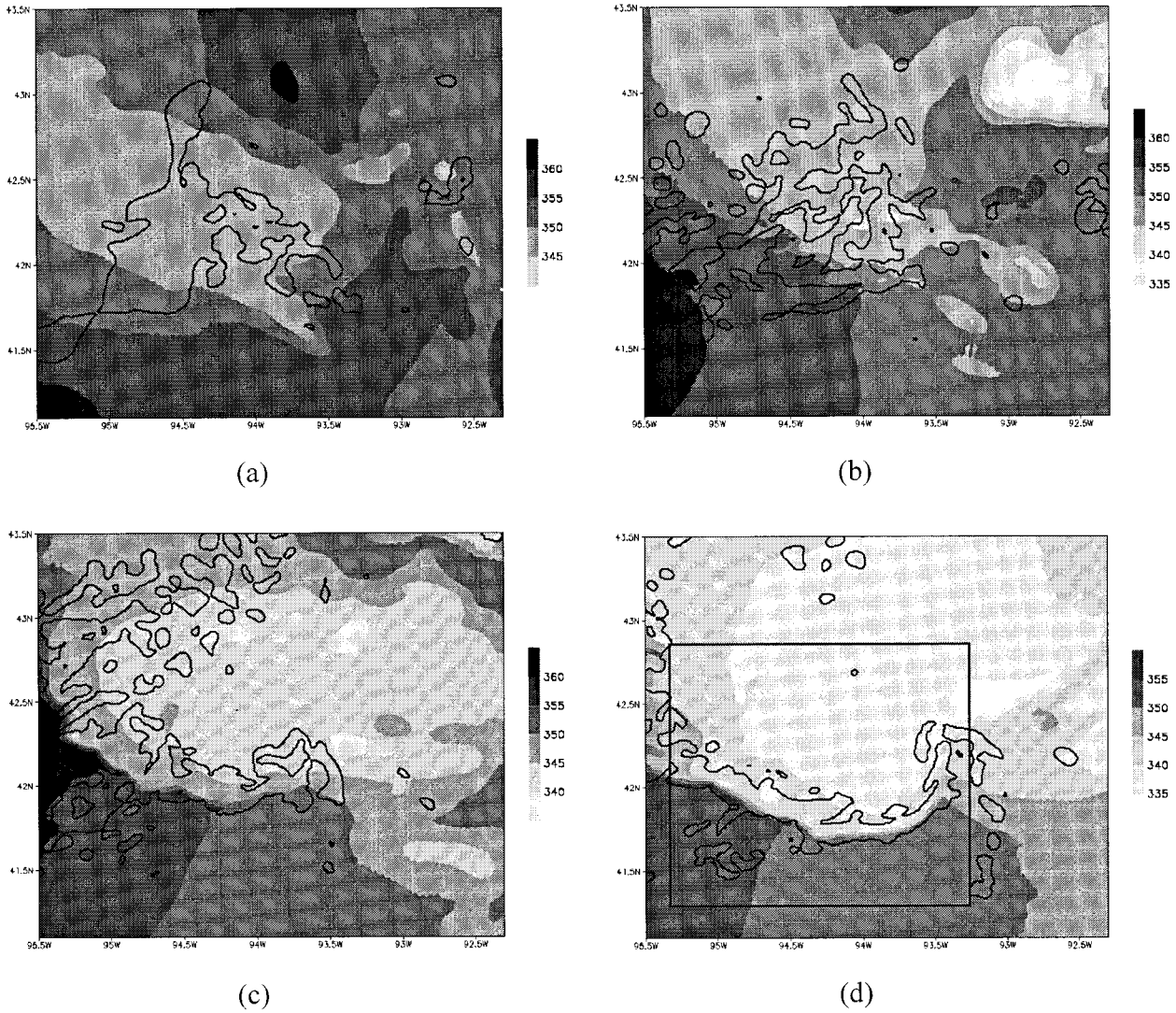

FIG. 20. Plot of θ_e (K, shaded) at $\sigma = 0.984$ level for (a) 0200, (b) 0400, (c) 0600, and (d) 0800 UTC 16 Jul. Contour encloses areas where cloud water mixing ratio at $\sigma = 0.7665$ level exceeds 0.1 g kg^{-1}. Box in (d) shows location of subdomain used in Fig. 21.

nitude of the balanced warm core of the vortex, thereby further lowering heights beneath the warm core. The low-level wind field adjusts to the changes in the mass field imposed from above, thereby producing convergence, spinup, and a cyclonic circulation closer to the surface.

This sequence of events can be elucidated by considering a form of the hypsometric equation (Hirschberg and Fritsch 1991):

$$\frac{\partial z(p_b)}{\partial t} = \frac{R}{g} \int_{p_b}^{p_l} \frac{\partial T_v}{\partial t}\, d\ \ln p, \qquad (3)$$

where p_l is a temporally invariant lid level assumed to be at sufficiently high levels where mean density changes and height changes are negligible. From Eq. (3), it is clear that net virtual warming (cooling) in the column above p_b will result in height falls (rises) at p_b [assuming $z(p_t)$ does not change]. Furthermore, the largest negative (positive) height tendencies will lie underneath columns of air in which the largest net virtual warming (cooling) is occurring.

This interpretation can be applied to an idealized schematic (Fig. 25a) depicting the thermal and momentum structure of an MCV that is in hydrostatic and gradient balance. In this schematic, a negative virtual temperature anomaly exists in the upper troposphere and lower stratosphere. From Eq. (3), the heights are locally higher within this virtually cold air and, because the system is balanced, an anticyclonic perturbation coexists with the locally higher heights. The strength of the positive height anomaly (and associated anticyclonic perturbation) reaches a peak at the base of the cold anomaly. With continued decreases in elevation, the positive virtual temperature anomaly offsets the cold anomaly

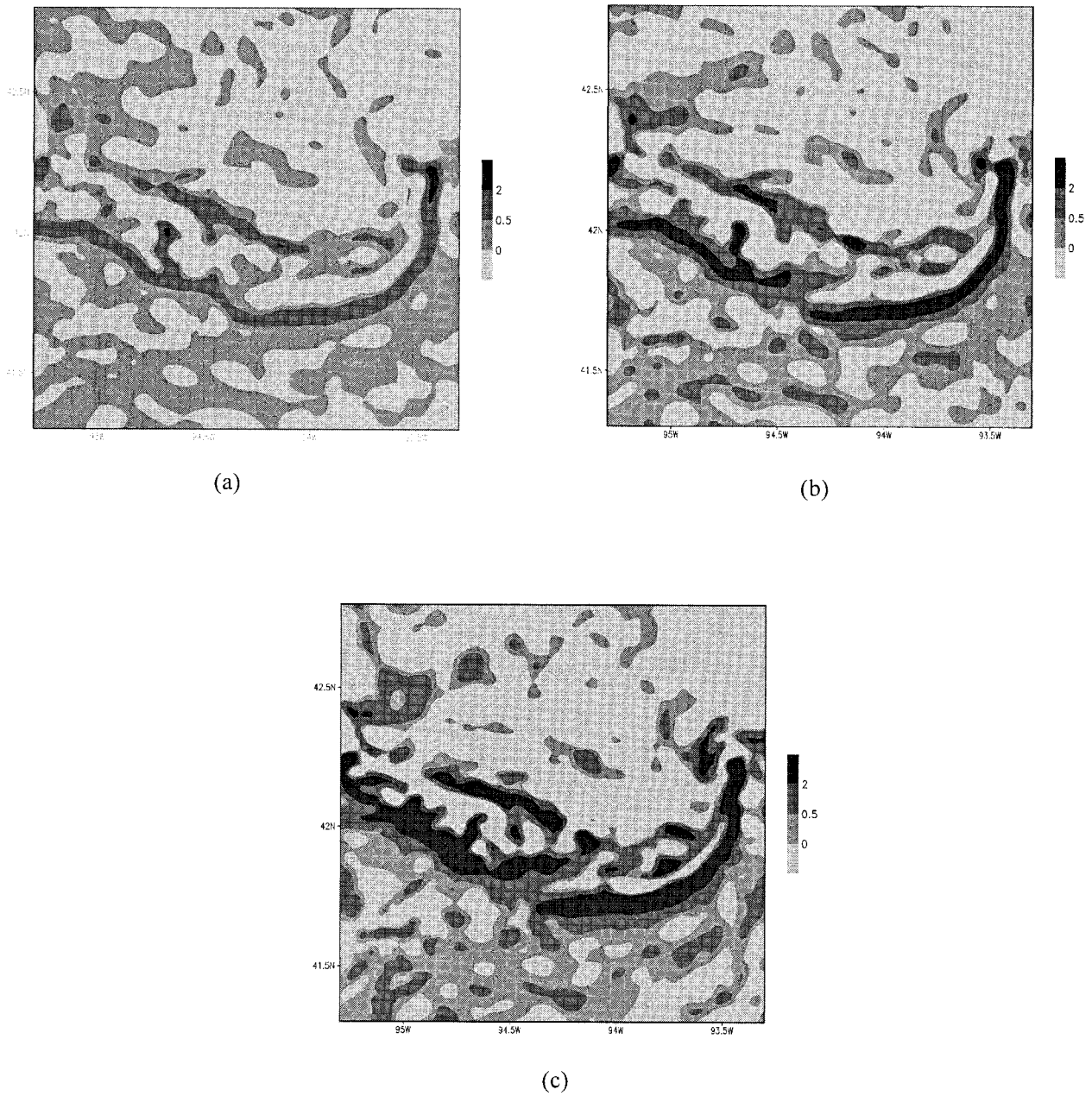

FIG. 21. Vertical motion (m s^{-1}) at 0800 UTC for the (a) $\sigma = 0.952$ level, (b) $\sigma = 0.8775$ level, and (c) $\sigma = 0.7665$ level. Shading denotes locations of upward motion.

above, eventually resulting in a level (labeled z_c in Fig. 25a) where the positive height anomaly switches to a negative anomaly. Beneath level z_c, and extending downward to level z_w (below the base of the warm anomaly), the *column-averaged* virtual temperature of the overlying layer is warmer than ambient values. Therefore, heights in the layer z_c to z_w are lower than ambient values and reach a peak departure from the large-scale environment at the base of the warm layer. From balance considerations, a cyclonic perturbation coexists with the negative height anomaly and is strongest at the base of the warm layer. Below the midlevel warm anomaly lies a surface-based layer of anomalously cold air. In the case of Fig. 25a, the surface-based cool layer is strong enough to offset the effects of the midlevel warm layer with the result that heights are anomalously higher from z_w to the surface. Thus, excluding the effects of surface friction, an anticyclonic perturbation prevails in the lower portion of this layer and reaches a peak at the surface. If the midlevel warm layer in Fig. 25a were somehow strengthened and there were no corresponding increases in the strength of the cold anomalies (Fig. 25b), z_w would

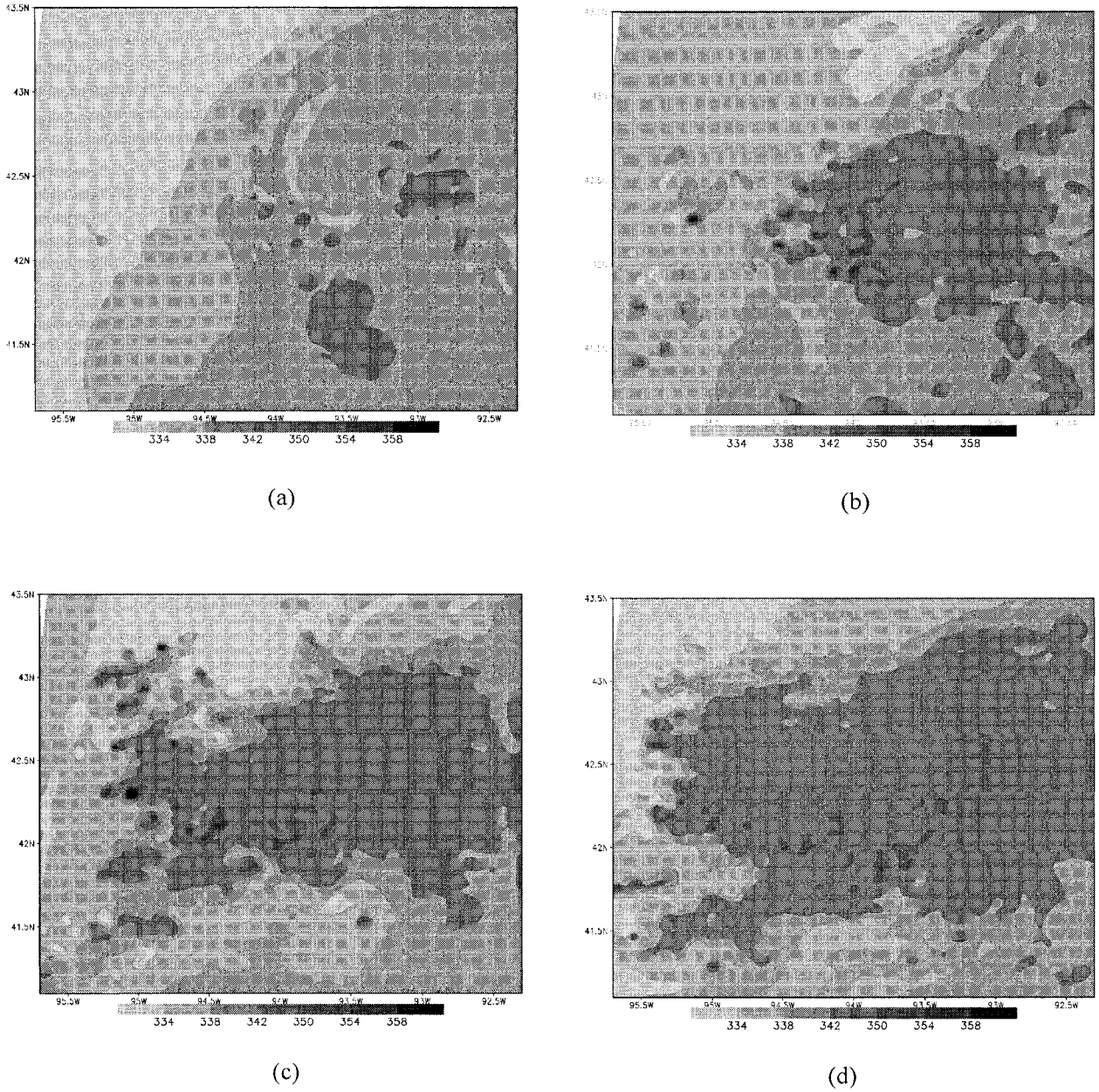

FIG. 22. Plot of θ_e (K, shaded) at the $\sigma = 0.336$ level at (a) 0200, (b) 0400, (c) 0600, and (d) 0800 UTC 16 Jul.

decrease. (In the example shown in Fig. 25b, z_w is actually below the surface, i.e., negative height anomalies exist at the surface.) From balance considerations, cyclonic vorticity would penetrate farther downward into the surface-based cold layer and, in this case, all the way to the surface.

The sequence of events required for cyclonic vorticity to develop down to the surface is governed by many factors. Three of the most important factors include the following.

1) *The onset of deep, moist convection:* The development of deep, moist convection within the vortex circulation is obviously important because of the perturbation to the vortex's mass field that arises through the release of latent heat. Where the convection occurs relative to the center of the vortex likely plays an important role in determining the impact of the convection on the height fields and, subsequently, the momentum fields of the vortex (assuming a suitable balance condition). Convection that occurs closer to the center of the existing vortex has been shown through previous studies to have a more significant impact on amplifying the vortex (e.g. Tracton 1973; Ritchie and Holland 1997; Montgomery and Eno-

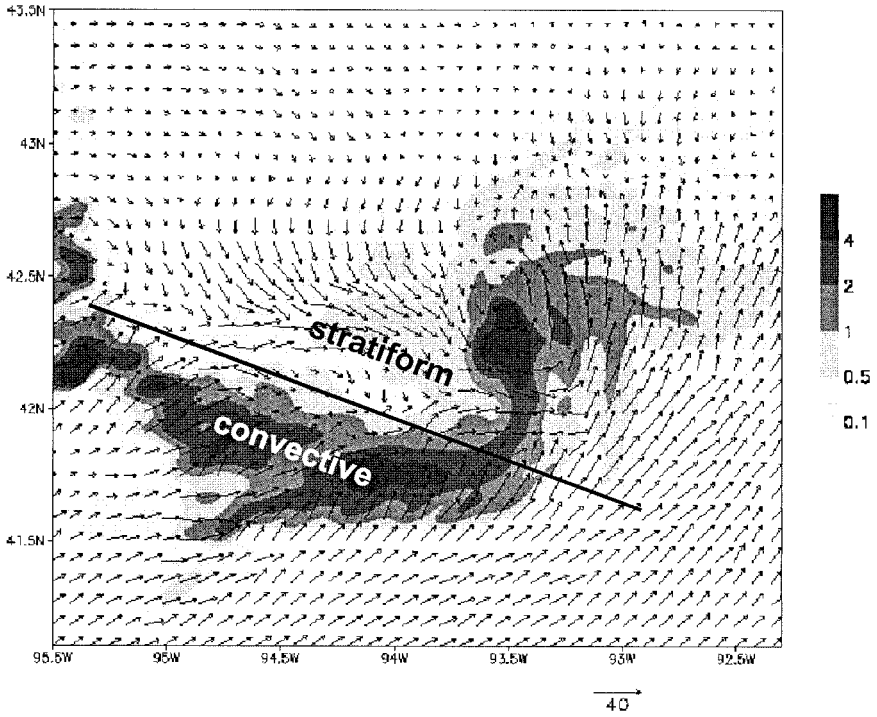

FIG. 23. Hourly total rainfall (shaded, cm h^{-1}) and wind vectors (m s^{-1}, maximum vector shown) at the $\sigma = 0.611$ level at 0900 UTC 16 Jul. Bold solid line denotes separation between ''convective'' and ''stratiform'' regions.

gonio 1998). In this simulation, parameterized convective heating covers a broad area, encompassing the center of the vortex during the redevelopment cycle. Grid-resolved heating, however, begins at locations between 50 and 100 km from the vortex center. This grid-resolved heating is so intense, though, that the center of the vortex soon shifts toward the location of maximum grid-resolved heating.

In addition to the importance of the location of convective heating, previous numerical studies have shown that the vertical profile of heating plays a crucial role in governing the amplification of the vortex (e.g., Anthes et al. 1983; Gyakum 1983). For example, whether the heating profile is typical of a convective or a stratiform heating profile determines whether the maximum PV production occurs in the lower or middle troposphere, respectively (Hertenstein and Schubert 1991). These profiles are dependent upon such factors as cloud-base height, precipitation efficiency, and motion of the convection relative to the environment, factors that are in turn dependent upon such environmental conditions as low- and midlevel relative humidity, wind shear, and static stability. In the simulation presented here, most of the heating directly tied to the vortex amplification occurs on the grid scale, and the vertical distribution of diabatic heating is typical of a convective heating profile. The magnitude of the heating is quite large, and may partially be attributed to the 18-km grid lengths used here. However, in the face of rapid destabilization via the transport of high-θ_e air in the low-level jet, it is reasonable to expect broad regions of intense convective heating. Whether or not the magnitudes of heating obtained here are reasonable requires direct comparisons between simulations and budget studies of observed systems, along with simulations with grid lengths smaller than 2 km. Such work awaits further study.

2) *Local reduction of the Rossby radius of deformation:* Implicit in all of the explanations provided here, from the discussions of the previous paragraphs to the idealized schematic shown in Fig. 25, is a state of balance between the vortex's mass (i.e., virtual temperature) fields and momentum fields. How the vortex responds to restore balance in the face of such processes as the release of latent heat within the system is what determines whether or not vortex amplification can proceed. What determines the nature of the response is the scale of the perturbation relative to the local Rossby radius of deformation. Such information can address the following questions: Will the area of diabatic *heating* result in a region of *warming* once balance is restored? What certainty is there that the wind field will adjust at all to the perturbations to the mass field brought on by the diabatic heating?

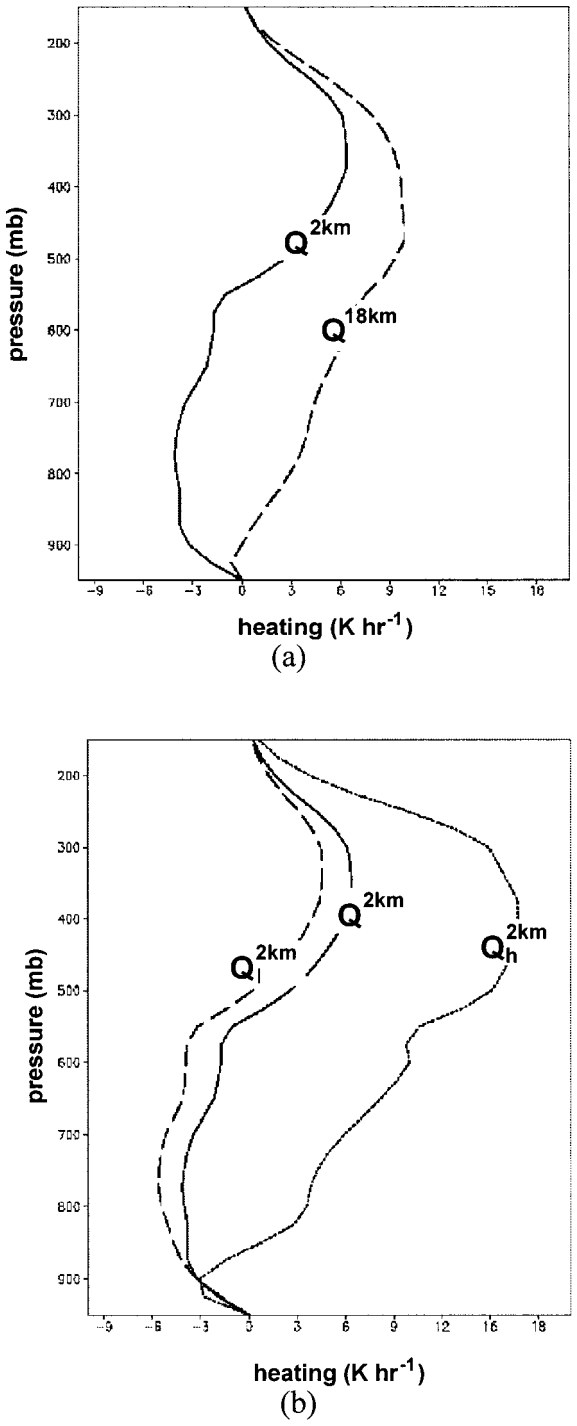

FIG. 24. (a) Profiles of grid-resolved diabatic heating (K h^{-1}) at 0900 UTC 16 Jul for 18-km simulation (Q^{18km}) at all locations where rain rate >0.1 cm h^{-1} and 2-km simulation (Q^{2km}) at all locations within the stratiform region (see Fig. 23) where rain rate >0.1 cm h^{-1}. (b) Profiles of grid-resolved diabatic heating at 0900 UTC for 2-km simulation at all locations within the stratiform region where rain rate >0.1 cm h^{-1} (Q^{2km}, same as Fig. 24a), all locations within the stratiform region where 0.1 cm h^{-1} ≤ rain rate < 1 cm h^{-1} (Q_l^{2km}), and all locations within the stratiform region where rain rate ≥ 1 cm h^{-1} (Q_h^{2km}).

In order for the diabatic heating to result in a net warming of the troposphere, and in order for the wind field to respond by spinning up cyclonic vorticity, the local Rossby radius must be reduced to a scale comparable to, or smaller than, the horizontal scale of the heating. A combination of factors can contribute to significantly reduce the values of the local Rossby radius. For example, existing cyclonic vorticity has long been known to improve the efficiency with which heating is manifested as a subsequent warming (e.g., Schubert et al. 1980). Moreover, the occurrence of diabatic heating within a saturated environment has been shown to reduce the Rossby radius by decreasing the effective static stability that governs the phase speed of the gravity waves responsible for the mass-field adjustment (Chen and Frank 1993). Soundings taken within the mesoscale environment of the vortex during the mature stage of the third convective cycle (Fig. 26) show that the middle and upper troposphere is saturated with nearly moist-neutral stability.

In a manner similar to that used by Chen and Frank (1993), the local Rossby radius associated with the third convective cycle can be computed. The general definition of the Rossby radius used in Schubert et al. (1980), Ooyama (1982), and Hack and Schubert (1986) is

$$L_R = \frac{C_g}{(f + \zeta)^{1/2}(f + 2VR^{-1})^{1/2}}, \tag{4}$$

where C_g is the phase speed of an inertia–gravity wave, f is the Coriolis parameter, ζ is the vertical component of relative vorticity, and V is the tangential component of the wind at the radius of curvature R. Using the relationship (Chen and Frank 1993)

$$C_g \propto NH, \tag{5}$$

where N is the Brunt–Väisälä frequency, the scale height of the disturbance H can be computed. In the early stages of the third convective cycle, the phase speed of the vertical motion maxima corresponding to the gravity waves created by the convection is about 30 m s^{-1}. This corresponds to a scale height H of 3.0 km, using $N = 10^{-2}$ s^{-1} for the unsaturated atmosphere within about 250 km of the convective system. Approximating the denominator of Eq. (4) by the absolute vorticity, the expression for the local Rossby radius becomes

$$L_R = \frac{NH}{f + \zeta}. \tag{6}$$

Equation (6) is used to compute the local Rossby radius during the third convective cycle. The values

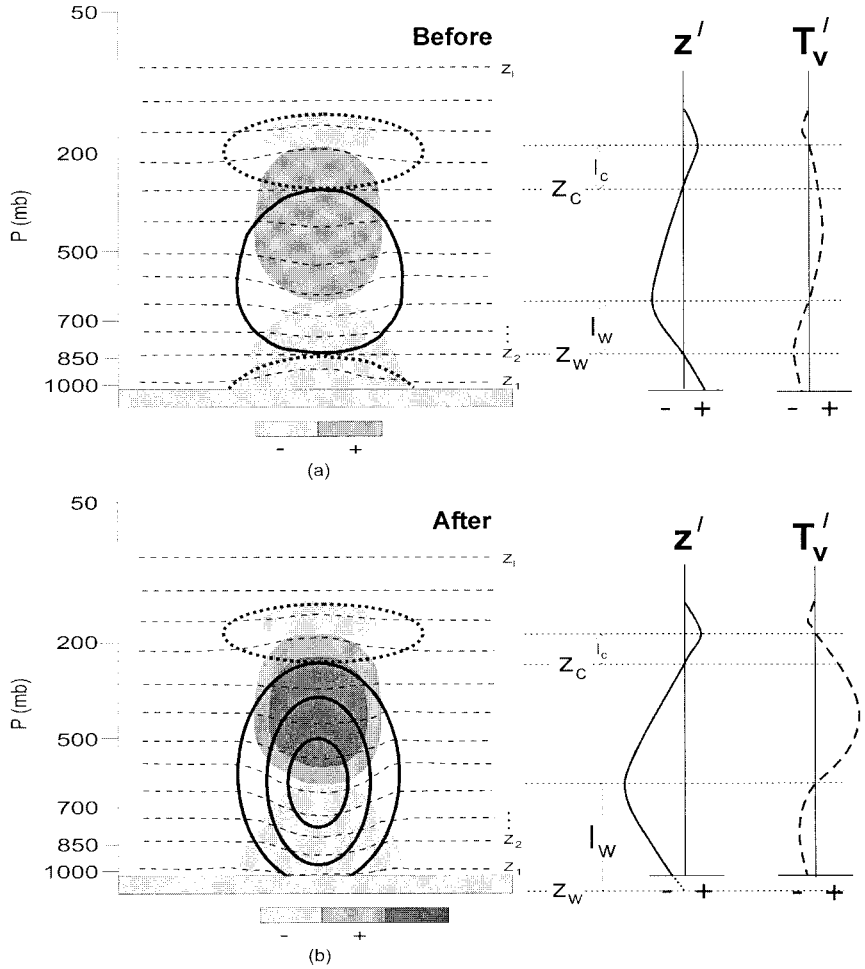

FIG. 25. (a) Idealized schematic showing height fields and virtual temperature and vorticity anomalies associated with an MCV in gradient wind balance. Shading denotes virtual temperature anomalies, thin dashed lines show height fields (z_l is the lid level), and heavy solid (dotted) lines show positive (negative) vorticity anomalies. Profiles to right show height (z', solid) and virtual temperature (T'_v, dashed) anomalies. (b) Same as (a) but with a stronger midlevel positive virtual temperature anomaly. ''Before'' and ''after'' refer to times before and after a convective redevelopment cycle, respectively.

for the static stability N are given by (Durran and Klemp 1982)

$$N_D = \left[\frac{g}{T}\left(\frac{dT}{dz} + \Gamma_d\right)\right]^{1/2}, \quad \text{for RH} < 100\%, \tag{7a}$$

and

$$N_M = \left[\frac{g}{T}\left(\frac{dT}{dz} + \Gamma_m\right)\left(1 + \frac{Lq_s}{RT}\right) - \frac{g}{1 + q_w}\frac{dq}{dz}\right]^{1/2}, \quad \text{for RH} = 100\%, \tag{7b}$$

where the terms in Eq. (7) assume the values they normally do. A very good approximation for N_M, which can more easily be computed from the model output, was also given in Durran and Klemp:

$$N_M = \left[g\left(\frac{1 + \dfrac{Lq_s}{RT}}{1 + \dfrac{\varepsilon L^2 q_s}{c_p RT^2}}\right) \times \left(\frac{d\ln\theta}{dz} + \frac{L}{C_p T}\frac{dq_s}{dz}\right) - \frac{dq_w}{dz}\right]^{1/2}, \quad \text{for RH} = 100\%, \tag{7c}$$

where $\varepsilon = R/R_v$. Figure 27 shows a time series (for the third convective cycle) of nine-point averages of relative humidity, relative vorticity, static stability, and the local Rossby radius of deformation centered on the midlevel (300–550-mb layer) potential vor-

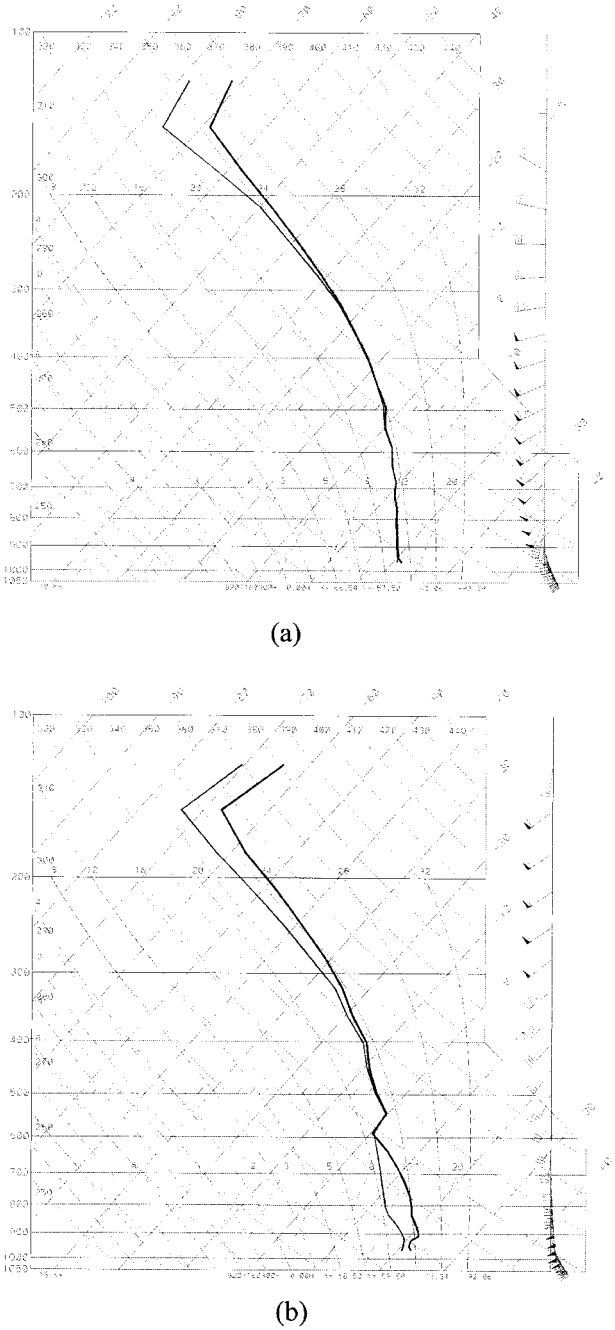

(a)

(b)

FIG. 26. Skew *T*–log*p* diagrams from 0900 UTC 16 Jul taken at (a) point A and (b) point B (see Fig. 11g for locations of points A and B).

ticity maximum. In the early stages of the convective cycle the environment of the vortex is subsaturated, with relative humidity values below 95%. As the convective cycle continues, though, the air becomes saturated, reducing the static stability by nearly 50%. As diabatic heating proceeds within this saturated, low-stability, high-vorticity environment, the local Rossby radius of deformation decreases from a maximum of 100 km at the beginning of the convective cycle to less than 20 km at the mature stage of the cycle. As this reduction is occurring, the vortex becomes more efficient at translating diabatic heating from the convection into a net warming of the atmosphere, with a subsequent increase in the midlevel cyclonic vorticity.

To the extent that this process involves a cooperative interaction between an existing vortex and moist convection, it is similar to the conditional instability of the second kind (CISK) mechanism described by Ooyama (1964) and Charney and Eliassen (1964). However, unlike CISK, cyclonic vorticity is not required in the lower troposphere. Therefore, the development of convection is not driven locally by the vortex itself (through Ekman pumping at the top of the boundary layer). Rather, convective development is forced by some external environmental factor, such as the low-level advection of high-θ_e air or the favorable positioning of an upper-level positive PV anomaly.

3) *Weakening of the surface-based cold pool:* Weakening the surface-based cold pool underneath the MCV aids in lowering the heights and increasing the cyclonic vorticity in the lower troposphere (assuming the wind field adjusts to the new mass field). This cold pool weakening can occur primarily through two mechanisms: 1) the enhancement of surface fluxes of heat and moisture, and 2) the weakening of cold downdrafts from the convective and stratiform precipitation. Surface fluxes will be enhanced if the MCV is over a warm water surface because of the strong air–sea temperature contrast, while middle- and lower-level moistening can occur through horizontal advection, large-scale upward motion in environments of lower-tropospheric convergence, or detrainment from convective towers.

6. Summary and concluding remarks

The effects of *repeated developments* of deep moist convection within a convectively generated mesoscale vortex were investigated using the Penn State–NCAR MM5. It was found that the MCV strengthened and grew downward in response to mid- and upper-tropospheric warming brought about by intense mesoscale diabatic heating. The strong heating occurred in a zone of powerful, saturated, mesoscale ascent as a low-level jet of high-θ_e air was forced to rise over a surface-based mesoscale cold pool created by previous convective developments and supplemented by ongoing parameterized and grid-resolved precipitation. Strong convective mixing within the mesoscale zone of ascent produced a deep, nearly moist-neutral layer that spanned an area several hundred kilometers in diameter. The formation of this broad area of low static stability effectively reduced the Rossby radius of deformation to less than the

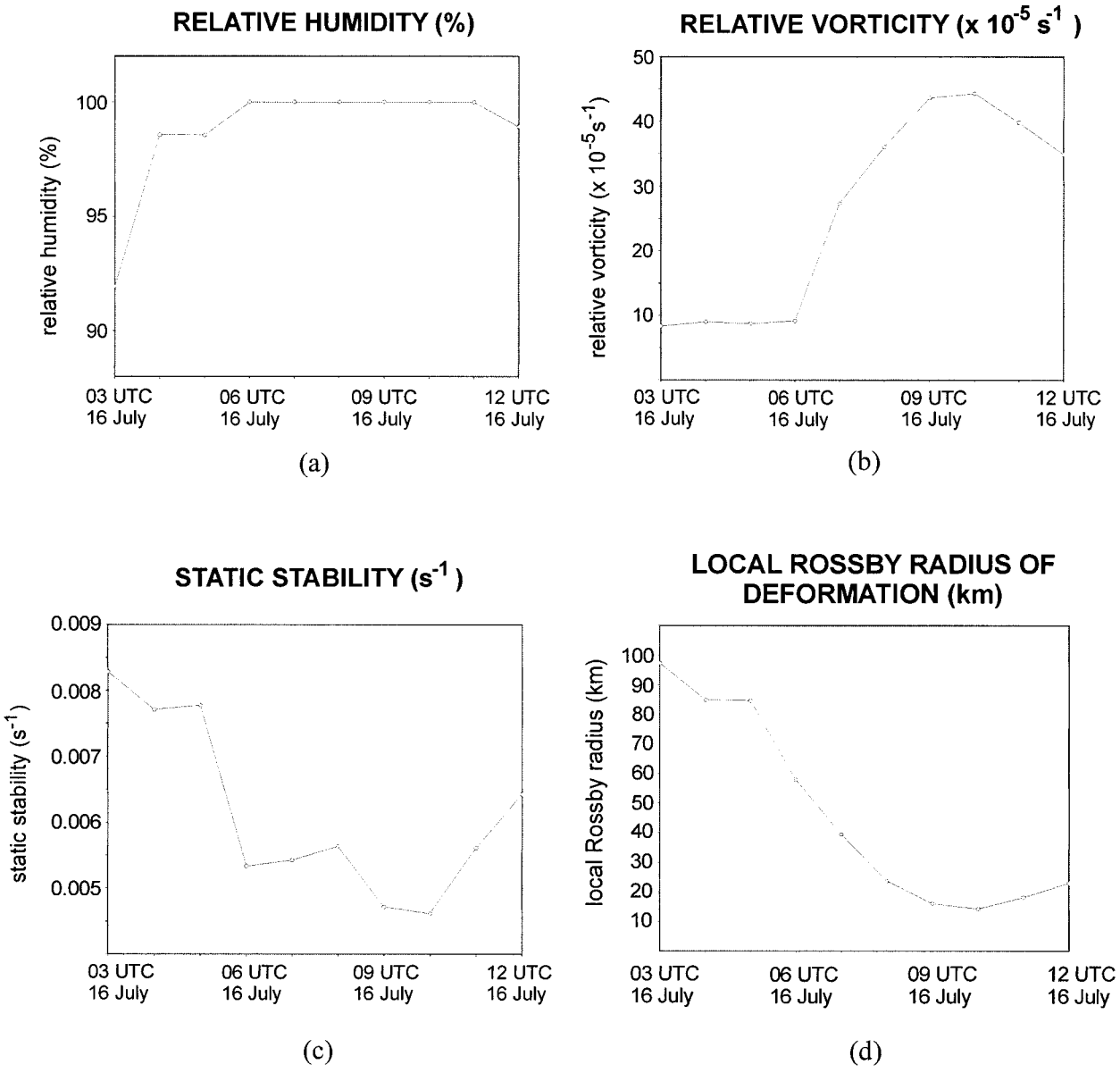

FIG. 27. Time series valid from 0300 to 1200 UTC 16 Jul of (a) relative humidity (%), (b) relative vorticity ($\times 10^{-5}$ s^{-1}), (c) static stability (s^{-1}), and (d) local Rossby radius of deformation (km) averaged over the 300–550-mb layer.

size of the moist near-neutral anomaly. This helped the system to retain much of the latent heating as a positive virtual warming in the mid- and upper troposphere. As the warm anomaly (originally created by the prior convective cycles) strengthened, the mid- and lower-tropospheric heights fell. Ultimately, the falling heights penetrated through the surface-based cold pool and created a low pressure anomaly at the surface. Convergence and increased cyclonic vorticity developed at the surface as the winds adjusted to the change in heights.

Inspection of the terms in the vorticity budget showed that tilting of cyclonic vorticity into the vertical was important in increasing midlevel vorticity in the early stages of the vortex amplification period. But the primary contributor to increasing cyclonic vorticity in the lower troposphere was stretching associated with low-level convergence forced by falling heights. Vertical advection in the strong mesoscale updraft was the dominant term in increasing cyclonic vorticity in the upper troposphere. At the same time that lower-tropospheric cyclonic vorticity was increasing, surface pressures underneath the vortex switched from being relatively high to relatively low. The increase of cyclonic vorticity in the lower troposphere and development of relatively low surface pressure occurred despite the fact that the surface-based layer of cold air was deepening and strengthening.

Since there was concern that the convective parameterization scheme utilized in the 18-km resolution control simulation may have inadvertently resulted in an ''unphysical'' formation of the midlevel mesoscale warm anomaly, it was deemed prudent to conduct a 2-km grid-mesh (cloud resolving) simulation of the development stage of the third convective cycle. It was found that the cloud-resolving simulation produced a midlevel mesoscale warm anomaly very similar to the structure that formed in the 18-km resolution simulation. The similarity of the structures and the manner in which they developed in both simulations supports the likelihood that the development of intense grid-resolved heating and the consequent midlevel warm anomaly in the 18-km simulation was not simply an artifact of deficiencies in the convective parameterization scheme. Rather, it appears to represent an important stage in the life cycle of some types of MCSs.

The results described above were obtained by investigating a multiconvective-cycle MCV that occurred over a midlatitude *land* surface in the summertime. Interestingly, observational studies of tropical cyclogenesis events (e.g., Zehr 1992) have found that multiple cycles of convective initiation are often required before a cyclonic circulation is observed at the surface, at which point a tropical system is identified as a tropical depression. Of course, many features that modulate the evolution of convective systems over midlatitude landmasses are quite different from those over the tropical oceans. For example, owing to the fact that the Coriolis parameter is much smaller in the Tropics, Rossby radii are typically much larger there. This makes it much harder for convective heating to be preserved as warming and translated to cyclonic vorticity production, and it highlights the importance of having background cyclonic vorticity, such as what would accompany a monsoon trough or easterly wave, to reduce the Rossby radius. It also suggests that more cycles of convection within a preexisting vortex may be necessary in order to moisten the environment and provide a favorable situation for saturated mesoscale ascent, with its substantially reduced Rossby radius, to occur.

Convection in tropical maritime regions is generally characterized by lower cloud bases and higher cloud- and subcloud-layer relative humidities compared to midlatitude environments. These factors typically lead to higher precipitation efficiencies, weaker downdrafts, and shallower cold pools in the Tropics. Furthermore, fluxes from the warm water surface would be enhanced in areas with cold moist downdrafts, further weakening the cold pools underneath the convective systems. The effect of these weaker cold pools would be to increase the low-level penetration of cyclonic vorticity associated with the midlevel virtual warm anomaly of MCVs—a favorable factor for tropical cyclogenesis. However, weaker cold pools can also have a detrimental effect for the subsequent development of convection, since the magnitude of the low-level lifting that accompanies the cold pool would also be weakened. On the other hand, locally strong low-level flow, such as the tropical maritime wind surges observed by Zehr (1992) during tropical cyclogenesis events, can compensate for the weaker cold pools since, other things being equal, faster flow would tend to produce stronger mesoscale ascent when it encounters a cold pool. The presence of strong low-level flow (relative to the movement of a convective system) is thought to be important since, in the present case, the strong mesoscale ascent was instrumental in creating the mesoscale warm anomaly that led to amplification of the system.

Acknowledgments. This work was supported by NSF Grants ATM-92-22017 and ATM-98-06309 and NASA Grant NAG 5-2927.

APPENDIX

Modifications to Model

Modifications that were included in the model reflected the need to more reliably represent various physical processes that were encountered in this simulation. Changes were made to various components of the planetary boundary layer parameterization scheme, convective parameterization scheme, and the model initialization scheme.

a. Planetary boundary layer parameterization scheme

Numerous changes are made to the PBL scheme in an attempt to make it more realistic for warm-season cases involving deep convection. The changes involve the impact that deep moist convection has on the surface energy budget equation:

$$C_g \frac{\partial T_g}{\partial t} = R_n - H_m - H_s - H_q, \qquad \text{(A1)}$$

where C_g is the thermal capacity of the slab per unit area, T_g is the temperature of the ground, R_n is the net radiative flux (longwave and shortwave), H_m is the heat flux into the substrate, H_s is the sensible heat flux into the atmosphere, and H_q is latent heat flux into the atmosphere.

1) SHORTWAVE ATTENUATION

The formulation for shortwave radiative flux at the surface used here is dependent upon grid-scale relative humidity within the column to obtain cloud fractional values at three different levels. Since subgrid-scale clouds can develop when the grid scale is subsaturated, the modification used here assumes a standard width and depth of convective cloud, as inferred from observational and modeling studies (e.g., Byers and Braham 1949; Browning 1981; Schlesinger 1994), to compute a cloud fraction for use in the attenuation scheme. Once

parameterized convection has ended, the convective cloud fraction is assumed to ramp back to the grid-scale value in a linear fashion over a 2-h time period.

2) Ground temperature tendency

Multiple processes are occuring at the surface when convection is active, all of which serve to cool the skin layer of the surface: for example, clouds obstruct the insolation, convective downdrafts cool the air at the surface, and rain falling from the cloud cools the ground through conduction as it encounters the surface. While most of these processes are accounted for by the physical parameterizations, no representation of the sensible cooling from the rainwater itself is currently available. In recognition of this deficiency, the scheme used in Zhang and Fritsch [1986, their Eq. (14)] is employed. While this formulation is admittedly crude, a comparison of simulated and observed low-level temperatures when deep convection was active indicated that the temperature evolution was more realistic when this formulation was included.

3) Moisture availability

To account for the moistening of the ground due to moist convection, the moisture availability is increased to a high value when parameterized convection is active. Once convection stops, the moisture availability is assumed to return to its background (i.e., climatological) state in a linear fashion over a time period of 6 h. This time period was chosen based on results of coupled soil hydrology–atmospheric boundary layer modeling studies (Sasamori 1970; McCumber and Pielke 1981).

b. Convective parameterization scheme

It has become evident from diagnostic studies (e.g., Leary and Houze 1980; Gamache and Houze 1983) that midlevel detrainment of mass and moisture from deep convective clouds is an important factor in guiding the development of some MCSs. However, in the Kain–Fritsch scheme, the amount of mass and moisture detrained from clouds in the low- and midlevels remains negligible in environments with a high convective available potential energy. To allow for enhanced detrainment rates from convective clouds, the detrainment scheme in the cloud model is modified to allow for values of detrainment that are proportional to values of entrainment. In this sense the modification is similar to the formulation of Frank and Cohen (1987). For these simulations the ratio of entrainment rates to detrainment rates is set to unity. This value falls within the range that was found by Frank and Cohen (1987) and Cohen and Frank (1987) to produce realistic anvil clouds.

c. Initialization scheme

1) Depiction of convective system

Several techniques are employed to include many of the features missed by the conventional initialization scheme. First, surface-based outflows from convection that is occurring at initialization time are incorporated. The technique, outlined by Stensrud and Fritsch (1994), consists of identifying areas where convective outflows exist, based on satellite and radar images and surface observations, and computing a perturbation sea level pressure field created by the convective system. An outflow temperature is determined from the local environment, and the depth of the outflow is calculated from the hydrostatic equation. These outflows are then inserted into the model initialization.

Another technique for improving the initialization of mesoscale features involves specifying an idealized thermodynamic structure in locations where organized deep convection is occurring at initialization time. The thermodynamic structure is based on many observational studies of such features (e.g., Houze 1977; Zipser 1977). Momentum fields are not altered from the conventional initialization, because no assumption regarding balance conditions seems appropriate given the limited observations of the system. Further, it is assumed that the thermodynamic stuctures, coupled with the forcing of parameterized convection by the radar data, will allow the model to create the relevant circulations on the mesoscale. Finally, since the purpose of this study is to examine the impacts of convection on the structure and evolution of mesoscale vortices, it seems unwise to bias the structure and evolution of this system by assuming an initial state for them. By not prescribing an initial vortex structure, the maximum impact of the model's primitive equations in generating such features is allowed.

2) Specification of cloud locations

To improve the initial specification of cloud locations, relative humidity profiles in the model are adjusted in regions where clouds are noted in the observations. The technique for accomplishing this is essentially a cruder version of the method used in Koch et al. (1997). Surface observations of cloud coverage and base are combined with satellite imagery to infer cloud depths, and relative humidities associated with these cloudy regions are based on the observed cloud cover. Bogus soundings are inserted into the model's analysis routines with these humidities specified, and a more accurate depiction of the moisture field is created.

3) Moisture availability modifications

Daily maps of precipitation during the week preceding model initialization are used to outline regions where moisture availability may depart from the sea-

sonal averages used in the conventional initialization scheme. Surface temperature and dewpoint evolution during the daytime hours in the model are also compared with observations to gauge whether modifications should be made. Furthermore, in locations where upper-air soundings are available and clouds are not present, the mixed-layer structure of the observed PBL is compared with the simulated PBL to determine where moisture availability should be increased or decreased. For regions where an increase is deemed necessary, values of moisture availability are increased 50%, while for locations where a decrease is deemed necessary, values are reduced 25%. The resulting surface temperature and moisture evolutions and PBL structures in the model are improved by this method.

d. Relative importance of modifications

The multitude of modifications described above and in section 2 all have varying degrees of importance in simulating the observed evolution of events. The radar nudging scheme is the most important in placing the third convective cycle in the proper location and amplifying the midlevel vortex (Rogers et al. 2000). The outflow specification scheme and thermodynamic profile specification near convection, while crude, are crucial in producing the evolution of the first convective cycle and remnant low-level cold pool. The remaining modifications are less important in producing a successful simulation. The moisture availability modifications help in producing a moist PBL upstream and prior to the onset of the third convective cycle. The detrainment parameter and cloud location specifications are the least important in contributing to the success of this simulation. That is not to say, however, that these modifications would not be more important in other simulations.

REFERENCES

Anthes, R. A., and T. T. Warner, 1978: Development of hydrodynamic models suitable for air pollution and other mesometeorological studies. *Mon. Wea. Rev.,* **106,** 1045–1078.

——, Y.-H. Kuo, and J. R. Gyakum, 1983: Numerical simulations of a case of explosive marine cyclogenesis. *Mon. Wea. Rev.,* **111,** 1174–1188.

Barnes, S. L., 1964: A technique for maximizing details in numerical weather map analysis. *J. Appl. Meteor.,* **3,** 396–409.

Bartels, D. L., and R. A. Maddox, 1991: Midlevel cyclonic vortices generated by mesoscale convective systems. *Mon. Wea. Rev.,* **119,** 104–118.

Benjamin, S. G., and T. N. Carlson, 1986: Some effects of surface heating and topography on the regional severe storm environment. Part I: Three dimensional simulation. *Mon. Wea. Rev.,* **114,** 307–329.

Bister, M., and K. A. Emanuel, 1997: The genesis of Hurricane Guillermo: TEXMEX analyses and a modeling study. *Mon. Wea. Rev.,* **125,** 2662–2682.

Blackadar, A. K., 1979: High-resolution models of the planetary boundary layer. *Advances in Environmental Science and Engineering,* J. Pfafflin and E. Ziegler, Eds., Vol. 1, No. 1, Gordon and Breach, 50–85.

Bosart, L. F., and F. Sanders, 1981: The Johnstown flood of July 1977: A long-lived convective storm. *J. Atmos. Sci.,* **38,** 1616–1642.

Brandes, E. A., 1990: Evolution and structure of the 6–7 May 1985 mesoscale convective system and associated vortex. *Mon. Wea. Rev.,* **118,** 109–127.

Browning, K. A., 1981: Morphology and classification of middle-latitude thunderstorms. *Thunderstorm Morphology and Dynamics,* E. Kessler, Ed., University of Oklahoma Press, 133–152.

Byers, H. R., and R. R. Braham, 1949: The Thunderstorm Project. U.S. Weather Bureau, U.S. Department of Commerce, Washington, DC, 287 pp. [NTIS PB 234515.]

Charney, J. G., and A. Eliassen, 1964: On the growth of the hurricane depression. *J. Atmos. Sci.,* **31,** 1241–1255.

Chen, S. S., and W. M. Frank, 1993: A numerical study of the genesis of extratropical convective mesovortices. Part I: Evolution and dynamics. *J. Atmos. Sci.,* **50,** 2401–2426.

Cohen, C., and W. M. Frank, 1987: Simulation of tropical convective systems. Part II: Simulations of moving cloud lines. *J. Atmos. Sci.,* **44,** 3800–3820.

Cotton, W. R., M.-S. Lin, R. L. McAnelly, and C. J. Tremback, 1989: A composite model of mesoscale convective complexes. *Mon. Wea. Rev.,* **117,** 765–783.

Farfan, L. M., and J. A. Zehnder, 1997: Orographic influence on the synoptic-scale circulations associated with the genesis of Hurricane Guillermo (1991). *Mon. Wea. Rev.,* **125,** 2683–2698.

Frank, W. M., and C. Cohen, 1987: Simulation of tropical convective systems. Part I: Cumulus parameterization. *J. Atmos. Sci.,* **44,** 3787–3799.

Fritsch, J. M., J. D. Murphy, and J. S. Kain, 1994: Warm core vortex amplification over land. *J. Atmos. Sci.,* **51,** 1780–1807.

Gamache, J. F., and R. A. Houze, 1983: Water budget of a mesoscale convective system in the tropics. *J. Atmos. Sci.,* **40,** 1835–1850.

Grell, G. A., J. Dudhia, and D. R. Stauffer, 1994: A description of the fifth-generation Penn State/NCAR mesoscale model (MM5). NCAR Tech. Note NCAR/TN-398 + 1A, 107 pp.

Gyakum, J. R., 1983: On the evolution of the *QE II* storm. II: Dynamic and thermodynamic structure. *Mon. Wea. Rev.,* **111,** 1156–1173.

Hack, J. J., and W. H. Schubert, 1986: Nonlinear response of atmospheric vortices to heating by organized cumulus convection. *J. Atmos. Sci.,* **43,** 1559–1573.

Harr, P. A., R. L. Elsberry, and J. C. L. Chan, 1996: Transformation of a large monsoon depression to a tropical storm during TCM-93. *Mon. Wea. Rev.,* **124,** 2625–2643.

Hertenstein, R. F. A., and W. H. Schubert, 1991: Potential vorticity anomalies associated with squall lines. *Mon. Wea. Rev.,* **119,** 1663–1672.

Hirschberg, P. A., and J. M. Fritsch, 1991: Tropopause undulations and the development of extratropical cyclones. Part I: Overview from a cyclone event. *Mon. Wea. Rev.,* **119,** 496–517.

Hoskins, B. J., M. E. McIntyre, and A. W. Robertson, 1985: On the use and significance of isentropic potential vorticity maps. *Quart. J. Roy. Meteor. Soc.,* **111,** 877–946.

Houze, R. A., Jr., 1977: Structure and dynamics of a tropical squall line system. *Mon. Wea. Rev.,* **105,** 1540–1567.

Johnson, R. H., 1984: Partitioning tropical heat and moisture budgets into cumulus and mesoscale components: Implications for cumulus parameterization. *Mon. Wea. Rev.,* **112,** 1590–1601.

——, and D. L. Bartels, 1992: Circulations associated with a mature-to-decaying midlatitude mesoscale convective system. Part II: Upper-level features. *Mon. Wea. Rev.,* **120,** 1301–1320.

Johnston, E. C., 1982: Mesoscale vorticity centers induced by mesoscale convective complexes. Preprints, *Ninth Conf. on Weather Forecasting and Analysis,* Seattle, WA, Amer. Meteor. Soc., 196–200.

Kain, J. S., and J. M. Fritsch, 1990: A one-dimensional entraining/detraining plume model and its application in convective parameterization. *J. Atmos. Sci.,* **47,** 2784–2802.

——, and ——, 1993: Convective parameterization for mesoscale models: The Kain–Fritsch scheme. *The Representation of Cu-*

mulus Convection in Numerical Models, Meteor. Monogr., No. 46, Amer. Meteor. Soc., 165–170.

——, and ——, 1998: Multiscale convective overturning in mesoscale convective systems: Reconciling observations, simulations, and theory. *Mon. Wea. Rev.,* **126,** 2254–2273.

Koch, S. E., A. Ahmet, and J. T. McQueen, 1997: The influence of mesoscale humidity and evapotranspiration fields on a model forecast of a cold-frontal squall line. *Mon. Wea. Rev.,* **125,** 384–409.

Laing, A. G., and J. M. Fritsch, 1993a: Mesoscale convective complexes over the Indian monsoon region. *J. Climate,* **6,** 911–919.

——, and ——, 1993b: Mesoscale convective complexes in Africa. *Mon. Wea. Rev.,* **121,** 2254–2263.

Leary, C. A., and R. A. Houze, 1980: The contribution of mesoscale motions to the mass and heat fluxes of an intense tropical convective system. *J. Atmos. Sci.,* **37,** 784–796.

——, and E. N. Rappaport, 1987: The life cycle and internal structure of a mesoscale convective complex. *Mon. Wea. Rev.,* **115,** 1503–1527.

Liu, Y., D.-L. Zhang, and M. K. Yau, 1997: A multiscale numerical study of Hurricane Andrew (1992). Part I: Explicit simulation and verification. *Mon. Wea. Rev.,* **125,** 3073–3093.

Maddox, R. A., 1980a: Mesoscale convective complexes. *Bull. Amer. Meteor. Soc.,* **61,** 1374–1387.

——, 1980b: An objective technique for separating macroscale and mesoscale features in meteorological data. *Mon. Wea. Rev.,* **108,** 1108–1121.

——, 1983: Large-scale meteorological conditions associated with midlatitude, mesoscale convective complexes. *Mon. Wea. Rev.,* **111,** 126–140.

McCumber, M. C., and R. A. Pielke, 1981: Simulation of the effects of surface fluxes of heat and moisture in a mesoscale numerical model. *J. Geophys. Res.,* **86,** 9929–9938.

Menard, R. D., and J. M. Fritsch, 1989: An MCC-generated inertially stable warm core vortex. *Mon. Wea. Rev.,* **117,** 1237–1261.

Miller, D., and J. M. Fritsch, 1991: Mesoscale convective complexes in the western Pacific region. *Mon. Wea. Rev.,* **119,** 2978–2992.

Montgomery, M. T., and J. Enagonio, 1998: Tropical cyclogenesis via convectively forced vortex Rossby waves in a three-dimensional quasigeostrophic model. *J. Atmos. Sci.,* **55,** 3176–3207.

Ooyama, K., 1964: A dynamical model for the study of tropical cyclone development. *Geofis. Int.,* **4,** 187–198.

——, 1982: Conceptual evolution of the theory and modeling of the tropical cyclone. *J. Meteor. Soc. Japan,* **60,** 369–379.

Purdom, J. F. W., 1976: Some uses of high-resolution GOES imagery in the mesoscale forecasting of convection and its behavior. *Mon. Wea. Rev.,* **104,** 1474–1483.

Ritchie, E. A., and G. J. Holland, 1997: Scale interactions during the formation of Typhoon Irving. *Mon. Wea. Rev.,* **125,** 1377–1396.

Rogers, R. F., J. M. Fritsch, and W. C. Lamber, 2000: A simple technique for using radar data in the dynamic initialization of a mesoscale model. *Mon. Wea. Rev.,* **128,** 2560–2574.

Sasamori, T., 1970: A numerical study of atmospheric and soil boundary layers. *J. Atmos. Sci.,* **27,** 1122–1137.

Schlesinger, R. E., 1994: Heat, moisture, and momentum budgets of isolated deep midlatitude and tropical convective clouds as diagnosed from threee-dimensional model output. Part I: Control experiments. *J. Atmos. Sci.,* **51,** 3649–3673.

Schubert, W. H., J. J. Hack, P. L. Silva Dias, and S. R. Fulton, 1980: Geostrophic adjustment in an axisymmetric vortex. *J. Atmos. Sci.,* **37,** 1464–1484.

Shapiro, L. J., and M. T. Montgomery, 1993: A three-dimensional balance theory for rapidly rotating vortices. *J. Atmos. Sci.,* **50,** 3322–3335.

Simpson, J., E. A. Ritchie, G. J. Holland, J. Halverson, and S. Stewart, 1997: Mesoscale interactions in tropical cyclone genesis. *Mon. Wea. Rev.,* **125,** 2643–2661.

Stensrud, D. J., and J. M. Fritsch, 1994: Mesoscale convective systems in weakly forced large-scale environments. Part II: Generation of a mesoscale initial condition. *Mon. Wea. Rev.,* **122,** 2068–2083.

Tracton, M. S., 1973: The role of cumulus convection in the development of extratropical cyclones. *Mon. Wea. Rev.,* **101,** 573–593.

Trier, S. B., and E. B. Parsons, 1993: Evolution of environmental conditions preceding the development of a nocturnal mesoscale convective complex. *Mon. Wea. Rev.,* **121,** 1078–1098.

Tuleya, R. E., and Y. Kurihara, 1981: A numerical study on the effects of environmental flow on tropical storm genesis. *Mon. Wea. Rev.,* **109,** 2487–2506.

Velasco, I., and J. M. Fritsch, 1987: Mesoscale convective complexes in the Americas. *J. Geophys. Res.,* **92,** 9591–9613.

Weisman, M. L., W. C. Skamarock, and J. B. Klemp, 1997: The resolution dependence of explicitly modeled convective systems. *Mon. Wea. Rev.,* **125,** 527–548.

Williams, D. T., 1963: The thunderstorm wake of May 4, 1961. National Severe Storms Project. Rep. No. 18, U.S. Dept. of Commerce, Washington, DC, 23 pp. [NTIS PB 168223.]

Zehr, R. M., 1992: Tropical cyclogenesis in the western North Pacific. NOAA Tech. Rep. NESDIS 61, 181 pp. [Available from NOAA/NESDIS, 5200 Auth Rd., Washington, DC 20233.]

Zhang, D.-L., 1989: The effect of parameterized ice microphysics on the simulation of vortex circulation with a mesoscale hydrostatic model. *Tellus,* **41A,** 132–147.

——, and R. A. Anthes, 1982: A high-resolution model of the planetary boundary layer-sensitivity tests and comparisons with SESAME-79 data. *J. Appl. Meteor.,* **21,** 1594–1609.

——, and J. M. Fritsch, 1986: Numerical simulation of the meso-β scale structure and evolution of the 1977 Johnstown flood. Part I: Model description and verification. *J. Atmos. Sci.,* **43,** 1913–1943.

——, and ——, 1987: Numerical simulation of the meso-β scale structure and evolution of the 1977 Johnstown flood. Part II: Inertially stable warm-core vortex and the mesoscale convective complex. *J. Atmos. Sci.,* **44,** 2593–2612.

——, and N. Bao, 1996: Oceanic cyclogenesis as induced by a mesoscale convective system moving offshore. Part I: A 90-h real-data simulation. *Mon. Wea. Rev.,* **124,** 1449–1469.

Zipser, E. J., 1977: Mesoscale and convective-scale downdrafts as distinct components of squall-line circulation. *Mon. Wea. Rev.,* **105,** 1568–1589.